

A MEASUREMENT OF $Z(\nu\bar{\nu})\gamma$ PRODUCTION AND A
SEARCH FOR NEW PHYSICS IN MONOPHOTON EVENTS
USING THE CMS DETECTOR AT THE LHC

by

James Joseph Buchanan

A dissertation submitted in partial fulfillment of
the requirements for the degree of

Doctor of Philosophy
(Physics)

at the
UNIVERSITY OF WISCONSIN – MADISON
201X

Defended on T.B.D.

Dissertation approved by the following members of the Final Oral Committee:

Sridhara Dasu · Professor of Physics

Wesley Smith · Emeritus Professor of Physics

Matthew Herndon · Professor of Physics

T.B.D. · Professor of Physics

T.B.D. · Professor of T.B.D.

© Copyright James Joseph Buchanan 201X
All Rights Reserved

Abstract

This thesis presents several studies of monophoton final states using $35.9\text{ }fb^{-1}$ of 13 TeV proton–proton collision data collected by the CMS experiment at the LHC in 2016. The standard model $Z(\nu\bar{\nu})\gamma$ cross section is measured as a function of photon transverse momentum. No significant deviations from standard model predictions are observed. The results are also interpreted in the context of several new physics models. Limits are placed on coupling strengths of anomalous triple gauge couplings between photons and Z bosons, new particle masses in simplified models of dark matter, the suppression scale of a dark matter effective field theory model, and the graviton mass scale in a model of extra spatial dimensions.

Contents

Abstract	i
1 Introduction	1
1.1 Overview	1
1.2 Standard model of particle physics	2
1.3 $Z(\nu\bar{\nu})\gamma$ cross section	7
1.3.1 Previous measurements	10
1.4 Anomalous triple gauge couplings	11
1.4.1 Previous searches	13
1.5 Dark matter EFT and simplified models	17
1.5.1 Previous searches	21
1.6 ADD gravitons	25
1.6.1 Previous searches	27
2 The CMS experiment and the LHC	30
2.1 The LHC	30
2.1.1 Proton acceleration and collision	32
2.1.2 Collimation, magnets, and beam halo	34
2.2 The CMS experiment	36
2.2.1 Coordinate system	37

2.2.2	Superconducting solenoid and silicon tracking system	40
2.2.3	Electromagnetic calorimeter	43
2.2.4	Hadronic calorimeter	48
2.2.5	Muon systems	51
2.2.6	Trigger system	53
2.2.7	Luminosity measurement	55
3	Simulation	57
3.1	Parton distribution functions	57
3.2	Hard process generation	58
3.3	Parton showering and hadronization	61
3.4	Pileup and detector simulation	62
4	Object reconstruction	63
4.1	The particle-flow algorithm	63
4.2	Tracks and clusters	65
4.3	Photons and electrons	67
4.4	Muons	69
4.5	Jets and missing transverse momentum	70
5	Event selection	71
5.1	The monophoton signature and background sources	71
5.2	Trigger and p_T^{miss} filters	71
5.3	Photon	71
5.4	Missing transverse momentum	72
5.5	Lepton vetoes	72
5.6	Single electron control region	72

5.7	Single muon control region	72
5.8	Dielectron control region	72
5.9	Dimuon control region	72
6	Background estimation	73
6.1	Simulated backgrounds	73
6.2	Electron faking photon	73
6.3	Jet faking photon	73
6.4	Spikes	73
6.5	Beam halo	73
6.6	Transfer factors	73
6.7	Likelihood function	73
7	Results	74
7.1	$Z(\nu\bar{\nu})\gamma$ cross section	74
7.2	aTGC limits	74
7.3	DM simplified model limits	74
7.4	ADD limits	74
8	Conclusions	75
8.1	Summary	75
8.2	Outlook	75
	Bibliography	76

Chapter 1

Introduction

1.1 Overview

This thesis presents several analyses of event yields in “monophoton” final states, characterized by a single γ with high transverse momentum, along with an overall transverse momentum imbalance typically of equal magnitude and opposite direction to that of the photon. These analyses correspond to $35.9\text{ }fb^{-1}$ of 13 TeV proton-proton (pp) collision data collected in 2016 by the CMS detector at the LHC. A measurement of the production rate for the process $pp \rightarrow Z\gamma \rightarrow \nu\bar{\nu}\gamma$ is obtained and compared to predictions derived from the standard model (SM) of particle physics. No significant deviation from SM predictions is observed.

The predicted monophoton yield in several theories of physics beyond the SM (BSM) is higher than the SM prediction. This thesis examines two varieties of anomalous triple gauge coupling (aTGC), simplified models of dark matter (DM) interacting with SM matter via a vector or axial-vector mediator, an effective field theory (EFT) of DM interaction with γ and Z bosons, and a model of extra spatial dimensions. For each of these models, 95% confidence level (CL) limits are placed on relevant

parameters based on the observed collision data.

1.2 Standard model of particle physics

The *standard model* of particle physics is our current best mathematical framework for describing the behavior of elementary particles. The set of particles described by the SM is illustrated in Fig. 1.1, which groups them according to certain fundamental characteristics. Each particle has an intrinsic angular momentum known as spin, specified by the lower number in each square of Fig. 1.1. Spin can be an integer or half-integer, according to which the particle is classified as a *boson* or *fermion*, respectively. The fundamental fermions comprise six “flavors” of quarks—up (u), down (d), charm (c), strange (s), top (t), and bottom (b)—and six flavors of leptons: electron (e), muon (μ), and tau (τ), with three corresponding neutrinos (ν_e , ν_μ , ν_τ). Each of these has both a particle and an anti-particle variety; the quarks additionally come in three “colors”. We typically denote a particle by a letter, e.g. q for a generic quark; its antiparticle partner has an overbar, e.g. \bar{q} . The fundamental bosons comprise the H as well as the gauge bosons, in turn comprising the Z , photon (γ), two W s distinguished by their electric charge, and eight gluons (g) distinguished by a color-anticolor doublet.

The particles are related to one another through various classes of interactions, each of which has a corresponding charge whose sum must be conserved in any physical process. The electromagnetic and weak interactions correspond to electric charge and weak isospin, respectively. In Fig. 1.1, the value Q of the electric charge is specified by the middle number in each square. For quarks and leptons, weak isospin determines whether the particle is “up-type” (u , d , t , ν_e , ν_μ , ν_τ) or “down-type” (d , s , b , e , μ , τ). Weak isospin has a corresponding value T_3 : up-type fermions have

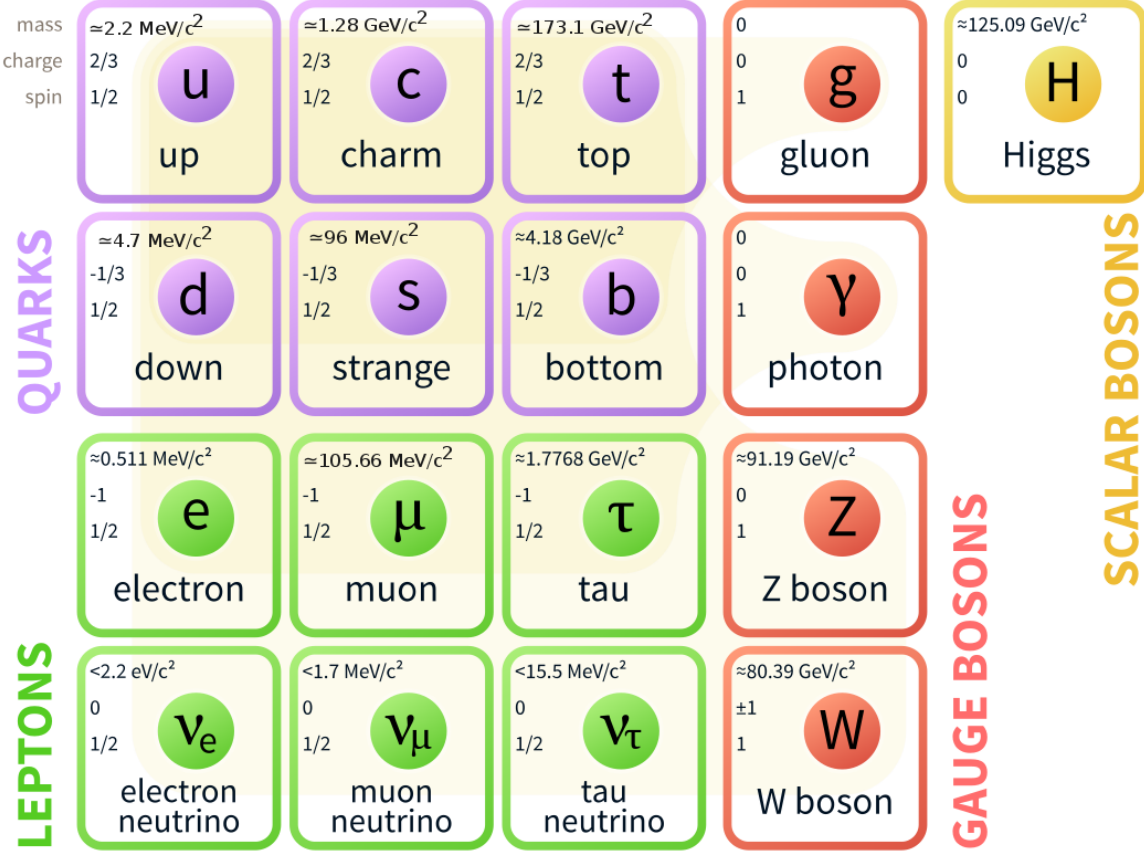


Figure 1.1: The particles of the Standard Model.

$T_3 = +1/2$, down-type fermions and the H have $T_3 = -1/2$, W^\pm have $T_3 = \pm 1$, and the other bosons have $T_3 = 0$. The three colors carried by quarks and gluons are associated with the strong interaction, described by the theory of *quantum chromodynamics* (QCD). The preceding discussion applies to normal (i.e. not anti-) particles; antiparticles carry opposite values of all the aforementioned charges.

These interactions lead to the relationships illustrated in Fig. 1.2, in which every linkage represents a direct *coupling*, which allows a particle at one end of the link to evolve directly into a particle at the other end. Particles with a nonzero electric charge are all coupled directly to the photon. The photon is coupled to the weak bosons (Z and W), which in turn couple to all of the fundamental fermions. The

gluons couple directly with each other and with the quarks. Particles that couple directly to the H have an intrinsic mass (specified by the top number in each square of Fig. 1.1) tied to the strength of their coupling. In the SM, any particle that does not couple directly to the H is massless.

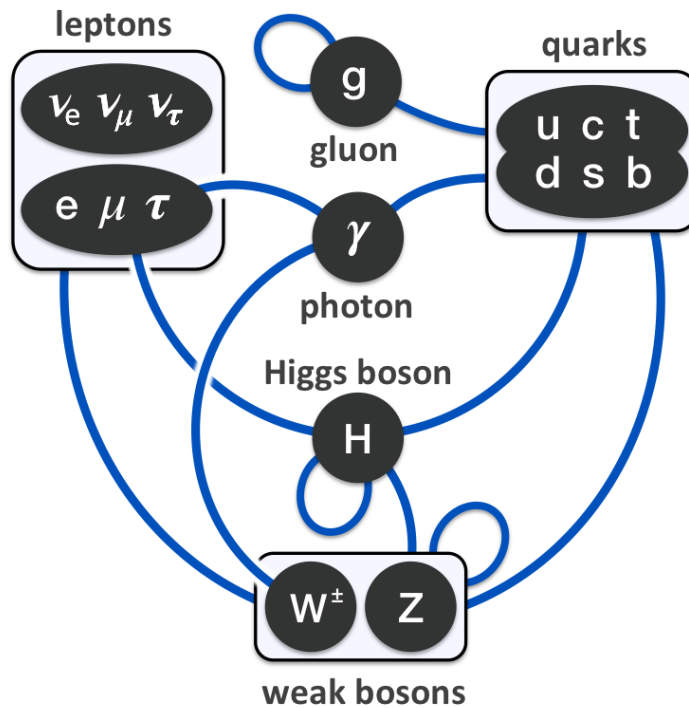


Figure 1.2: Standard Model couplings.

The full dynamics of the SM is encapsulated mathematically by a *Lagrangian* function. Particles correspond to operator terms appearing in the Lagrangian, and a coupling of one particle to another is described by multiplying their corresponding operators together. The SM Lagrangian is unchanged if all its fermion operators are multiplied by any complex number of the form $e^{iY\theta}$, where the *hypercharge* Y is a value that depends on the operator being multiplied. This is true even if θ is allowed to have different arbitrary values at different points in space and time, but

any operator with a nonzero Y couples to an additional operator denoted by B , and as a consequence the first derivatives of θ in space and time must also be subtracted from B . This deep level of invariance is called a *gauge symmetry*, with B the associated *gauge boson*. Multiplication by $e^{i\theta}$ is characterized by the group $U(1)$, so we say that the SM Lagrangian has a $U(1)_Y$ gauge symmetry associated with the B .

In a similar vein, the SM Lagrangian is unchanged if matching doublets of weak isospin up- and down-type operators are multiplied by unitary 2×2 matrices with determinant 1, described by the group $SU(2)$. Those with a nonzero weak isospin couple to every W^i ($i = 1, 2, 3$), which must receive their own balancing transformations if the fermion $SU(2)$ transformations are allowed to vary as a function of space and time. Hence we say that the SM Lagrangian has an $SU(2)$ gauge symmetry associated with the gauge bosons W^i .

The B and W^i 's also couple to the H , and the structure of this coupling constrains the physical states most easily accessed by these operators, corresponding to four distinct linear combinations of B and W^i . These combinations, which are themselves operators, are labeled Z , γ , W^+ , and W^- , and these are the operators describing the physical particles detected in experiments. In this manner, the electromagnetic and weak interactions are intertwined into the *electroweak* (EWK) interaction. The conserved electric charge Q emerges as the sum of T_3 with $\frac{1}{2}Y$.

Finally, the SM Lagrangian has an additional $SU(3)$ gauge symmetry associated with the eight gluons and color charge, described by QCD. Particles with color charge do not exist stably on their own, but rather are always observed in bound states called *hadrons*, in which the overall color charge state is invariant under any $SU(3)$ transformation. One such “colorless” configuration is the proton (p), which to a first approximation may be thought of as a bound state of two u quarks and one d quark.

However, the mass of the proton is much greater than the sum of the masses of

these three components, and this additional mass is associated with an effervescent “sea” of *partons*, transient particles swarming the proton that can only be distinguished at high energies. Known partons include gluons (carrying about 50% of the total momentum of a high-energy proton), all types of quark and antiquark, and photons. As a consequence, a high-energy collision between two protons can give rise to a $q\bar{q}$ interaction, which is the primary catalyst for all the processes studied below. A single parton carries some fraction of the total energy carried by the whole proton, so in general, partons collide with a lower interaction energy than that of the protons that carry them. The square of the center-of-mass energy of colliding protons is denoted by s , while that of a specific parton-parton interaction is denoted by \hat{s} .

This rapid overview of the SM necessarily elides many essential nuances of the underlying mathematical formalism. These are more fully documented in numerous comprehensive texts on the subject, e.g. [1–5].

The domain of applicability of the SM is quite substantial, encompassing every well-measured fundamental interaction of every verified fundamental particle. All SM particles have been conclusively observed, and no fundamental particles outside the SM have ever been conclusively observed. After decades of effort by thousands of researchers, no significant deviation from SM predictions has ever been confirmed in high-energy scattering experiments [6]. These efforts are extended here with studies of the relationship between Z and γ (sec. 1.3 and 1.4) at state-of-the-art precision. There are nevertheless many physical phenomena that the SM does not account for. The analyses presented here investigate the nature of gravitation (sec. 1.6), including the gravitational phenomenon known as DM (sec. 1.5), neither of which have an SM description.

1.3 $Z(\nu\bar{\nu})\gamma$ cross section

In a collision of two beams of particles, the average rate of any specific collision process is directly proportional to the number of particles in each of the colliding beams, to their density in the plane transverse to the beam direction, and to the average frequency at which particles are made to come into contact. These features determine the instantaneous *luminosity* \mathcal{L} of a pair of colliding beams, and the overall average rate of a given process may be written as $\sigma\mathcal{L}$, where σ is a constant of proportionality. Since σ has dimensions of area, it is called the *cross section*.

Cross sections may be calculated using *Feynman diagrams*. These are assembled by combining fundamental interaction vertices: the SM vertices relating the fermions and gauge bosons are listed in Fig. 1.3. Mathematical terms are assigned to Feynman diagrams according to a prescription known as the Feynman rules, which can be derived from the Lagrangian. This process results in a *matrix element* \mathcal{M}_i for each diagram i one wishes to consider. The cross section is proportional to the sum of $|\sum_i \mathcal{M}_i|^2 \rho$ over all kinematically consistent initial and final states of the given process¹. This method for calculating cross sections using Feynman diagrams is more fully described in refs. [1, 2]; a development in the context of quantum field theory is given in e.g. refs. [3–5].

The Feynman rule for a vertex includes a coupling constant g . These are typically less than 1 in high-energy collisions, meaning diagrams with additional vertices make smaller contributions to a cross section calculation. Whenever this is the case, we say that $|\sum_i \mathcal{M}_i|^2$ admits a *perturbative expansion*, in which the expression is organized as a sum of terms with increasing powers of $\alpha \propto g^2$, which make successively smaller contributions. Terms with the lowest powers of α are called leading order (LO) terms, followed by next-to-leading order (NLO), next-to-next-to-leading order (NNLO), etc.

¹ ρ is a function of the allowed kinematic parameters and is called the phase space factor.

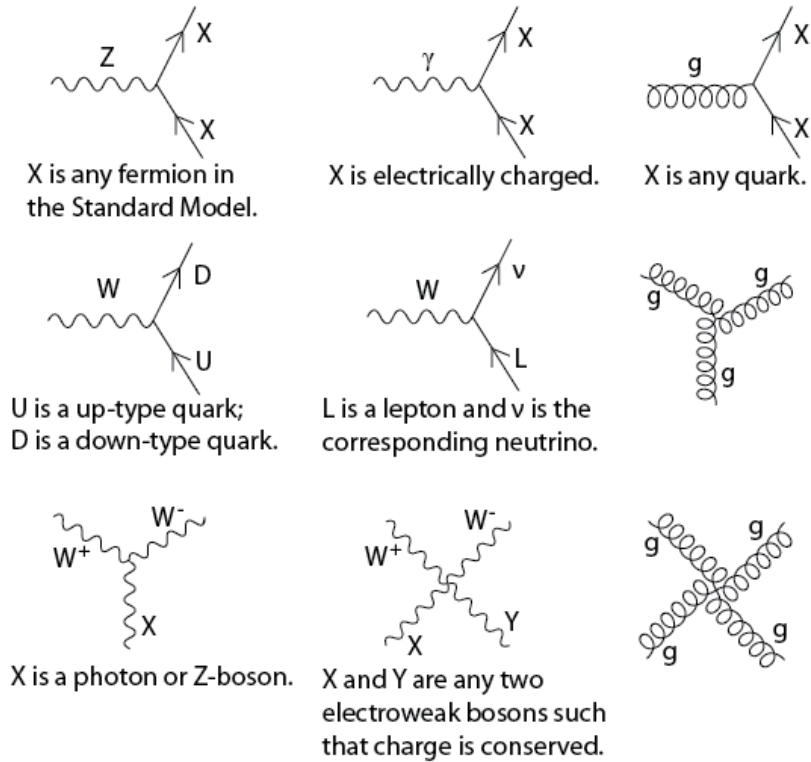


Figure 1.3: Fermion and gauge boson vertices of the standard model.

Diagrams with an internal loop contain at least one more vertex than equivalent diagrams without the loop, and therefore *tree-level* diagrams without any internal loops make the only contributions at LO (when they exist). Each class of interaction has its own characteristic coupling constant: an α without a subscript usually refers to the fine structure constant characterizing electromagnetic processes, while QCD is characterized by the strong coupling α_s .

In the SM, events with a monophoton signature arise at the LHC (Chap. 2) primarily from the process $q\bar{q} \rightarrow Z\gamma \rightarrow \nu\bar{\nu}\gamma$, where q is any single species of quark, ν is any single species of neutrino, and the neutrino-antineutrino pair arises from the decay of a short-lived Z boson. The leading tree-level diagram for this process is shown in Fig. 1.4(a). We typically abbreviate this process by reference to its final

state, $Z(\nu\bar{\nu})\gamma$. The final-state photon can be detected, but the neutrinos only interact with SM particles via the mediation of Z and W bosons, and these interactions are strongly suppressed by the high masses of those particles. Hence, neutrinos almost never interact directly with the LHC's detectors.

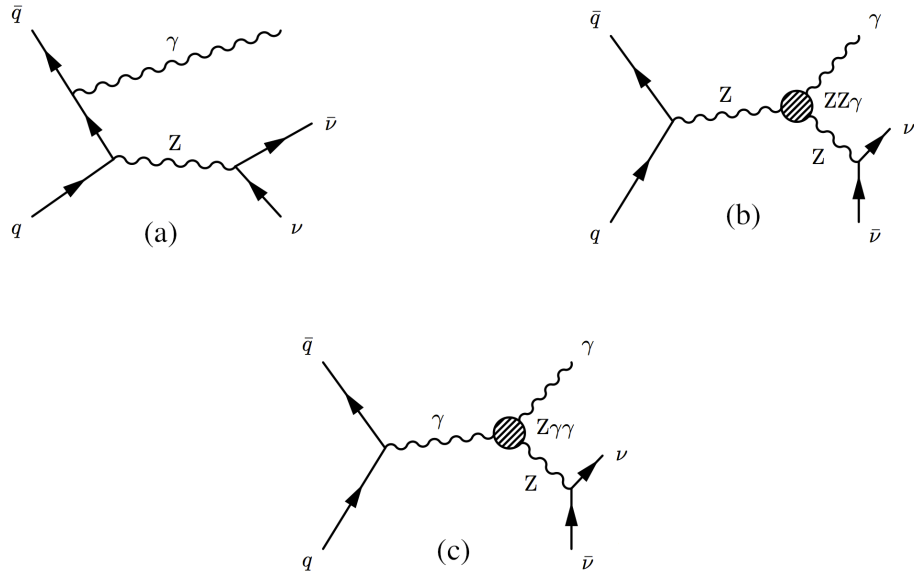


Figure 1.4: The leading Feynman diagrams for $Z(\nu\bar{\nu})\gamma$ production arising from pp collisions. Diagram (a) is the leading SM contribution. Diagrams (b) and (c) show contributions from aTGC vertices.

Their existence is instead inferred by their absence. In a collider experiment, the vectorial momentum transverse to the beam direction, \vec{p}_T , must sum to approximately zero in the reference frame of the detector. The negative vector sum of \vec{p}_T for all detected particles in an event is denoted \vec{p}_T^{miss} , and its magnitude p_T^{miss} must therefore be close to zero if all the particles in an event are reliably detected and their momenta are accurately measured. The only high-momentum SM particles that can't be reliably detected are neutrinos, so a large value of p_T^{miss} can be a sign of neutrino production. An event with a high- p_T detected photon, in which the \vec{p}_T^{miss} has a large

magnitude and points in a direction significantly different from that of the photon, is called a monophoton event, and it is expected that $Z(\nu\bar{\nu})\gamma$ processes are the main contributors of high- p_T monophoton events.

The theoretical SM value for the $Z(\nu\bar{\nu})\gamma$ cross section has been calculated to NLO in α and α_S [7,8]. The $Z(\nu\bar{\nu})\gamma$ process receives NLO contributions from 1-loop QCD and EWK diagrams, as well as tree-level diagrams with up to one additional radiated γ , q , or g . These contributions include diagrams with initial-state $q\bar{q}$, qg , and $\bar{q}g$ (with QCD and EWK corrections at NLO), as well as $q\gamma$, $\bar{q}\gamma$ (with EWK corrections at NLO) [8].

The calculation has also been done to NNLO in α_S alone, which includes contributions from tree-level diagrams with up to two extra radiated QCD partons (q or g), one-loop diagrams with up to one extra radiated QCD parton, and two-loop corrections. The initial-state QCD parton interactions include those listed among the NLO contributions above, as well as gg [9,10].

The exact values obtained from any such calculation depend on the specific initial and final states included. These restrictions (*cuts*) on events are informed by the operating conditions of the experiment one wishes to compare results with.

1.3.1 Previous measurements

Experiments at the LEP detector measured the cross section of $Z(\nu\bar{\nu})\gamma$ arising from e^+e^- collisions for \sqrt{s} up to ~ 200 GeV. The L3 experiment measured the cross section to be $5.1 \pm 0.3(\text{stat}) \pm 0.1(\text{syst}) \text{ pb}$ based on 175.6 pb^{-1} of collision data with an average $\sqrt{s} = 188.6$ GeV, compared to an SM prediction of $4.99 \pm 0.05(\text{stat})$ [11]. Looking at collision data at the same \sqrt{s} , but with different cuts, the OPAL experiment measured the cross section to be $2.52 \pm 0.13(\text{stat}) \pm 0.05(\text{syst}) \text{ pb}$ based on 177.3 pb^{-1} of data, compared to an SM prediction of $2.81 \pm 0.02(\text{stat}) \text{ pb}$ []. This set of SM predictions

were made up to $O(\alpha^2)$, but LO in α_S .

The D0 experiment at the Tevatron made the first observation of $Z(\nu\bar{\nu})\gamma$ arising from $p\bar{p}$ collisions in 2009. This yielded a cross section measurement of $32 \pm 9(\text{stat} + \text{syst}) \pm 2(\text{lumi}) \text{ fb}$ for a leading photon p_T above 90 GeV^2 , compared to an SM prediction of $39 \pm 4(\text{theory}) \text{ fb}$ computed to NLO in α_S [12].

Measurements of the cross section at higher values of p_T^γ have been performed by experiments examining pp collision data at the LHC. An analysis by the CMS experiment examining 19.6 fb^{-1} of data collected at $\sqrt{s} = 8 \text{ TeV}$ found the observed $Z(\nu\bar{\nu})\gamma$ cross section for $p_T^\gamma > 145 \text{ GeV}$ to be $52.7 \pm 2.1(\text{stat}) \pm 6.4(\text{syst}) \pm 1.4(\text{lumi}) \text{ fb}$, compared to an SM prediction of $40.7 \pm 4.9(\text{theory}) \text{ fb}$ calculated to NLO in α_S , and a prediction of $50.0_{-2.2}^{+2.4}(\text{theory})$ calculated to NNLO in α_S [13]. This comparison illustrates the need for NNLO precision at high p_T^γ .

The most precise measurement of the $Z(\nu\bar{\nu})\gamma$ cross section for p_T^γ and p_T^{miss} above 150 GeV currently comes from an analysis of 36.1 fb^{-1} of pp collision data collected by the ATLAS experiment at $\sqrt{s} = 13 \text{ TeV}$, with an observed cross section of $83.7_{-3.5}^{+3.6}(\text{stat})_{-6.2}^{+6.9}(\text{syst})_{-2.0}^{+1.7}(\text{lumi}) \text{ fb}$. The corresponding SM prediction, computed to NNLO in α_S using the MATRIX generator [14], is $78.6 \pm 0.4(\text{stat}) \pm 4.1(\text{syst}) \text{ fb}$ [15]. The cross section is shown in discrete ranges (bins) of leading photon p_T in Fig. 1.5.

None of these analyses report any significant deviation from the SM predictions.

1.4 Anomalous triple gauge couplings

Putative vertices joining three gauge bosons that are not found in the SM are known as aTGCs. For example, there is no fundamental SM vertex joining a single γ to a pair of Z s, or a single Z to a pair of γ s. A model describing the generic phenomenology

²The proper units for momentum are GeV/c , but the factor of c is often omitted for brevity, and this is the convention followed in this thesis.

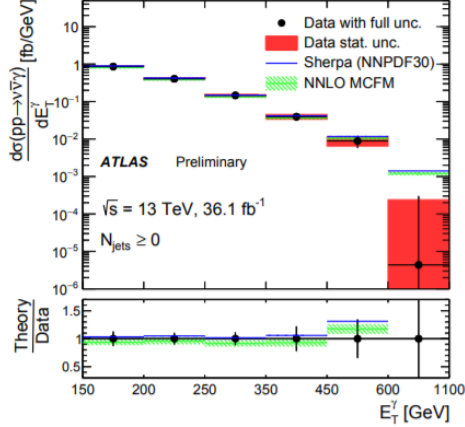


Figure 1.5: Cross section of $Z(\nu\bar{\nu})\gamma$ production plotted in bins of leading photon p_T (E_T^γ), as shown in [15]. The blue and green bands show the SM predictions derived from the Sherpa [16] and MCFM [17] generators, respectively.

of these aTGCs is developed in [18–20]. For an intermediate state $V = Z, \gamma$ decaying to a final state $Z\gamma$ pair, this model parametrizes the effective vertex interaction $ZV\gamma$ by a set of factors h_i^V (i from 1 to 4). Increasing the values of these parameters significantly increases the cross section of $Z(\nu\bar{\nu})\gamma$ processes, by allowing the reaction to proceed via the additional diagrams shown in Fig. 1.4(b),(c), in which the aTGC vertices are covered by opaque circles.

The circle could be thought of as masking a more detailed process taking place underneath. The SM admits processes that are predicted to contribute to this effective vertex, but all SM contributions to $h_{3,4}^V$ have at least one internal loop that could fit within the circle, and further loops are required for $h_{1,2}^V$ contributions [19]. As a consequence, the SM contribution to all eight h_i^V parameters is quite close to zero. The observation of a substantial nonzero value for any h_i^V would be a compelling sign of BSM physics.

The contributions to the $Z(\nu\bar{\nu})\gamma$ cross section coming from $h_{1,2}^V$ are independent of those from $h_{3,4}^V$ (for any V), and also nearly identical in magnitude, so without loss

of generality we only focus on scenarios for which $h_{3,4}^V$ are nonzero. The contributions from h_i^Z are largely independent of those from h_j^γ (for any i,j), so these are examined separately. However, the contributions from h_3^V are substantially correlated with those from h_4^V (and similarly for $h_{1,2}^V$), so we examine scenarios in which $h_{3,4}^V$ take on assorted pairs of values, both of which may be nonzero. The theoretical relationships between these parameters are explored in [19].

The neutrino decays of Z -bosons offer an especially good window on $ZZ\gamma$ and $Z\gamma\gamma$ aTGCs because the probability that a Z will decay into neutrinos is about six times higher than that of a decay into e^+e^- , or into $\mu^+\mu^-$. Furthermore, the probability of reconstructing a $Z(\nu\bar{\nu})\gamma$ event in a detector is typically higher than that of a charged lepton event. As a consequence, aTGC limits derived from neutral Z decays can be several times stronger than limits derived from charged Z decays when analyzing the same pp collision data sets (compare e.g. [21] and [22], based on 7 TeV LHC data; also Fig. 1.8, based on 8 TeV data). The decays of Z into $q\bar{q}$ (and thence to hadrons) are difficult to distinguish in practice from hadronic W decays [23].

1.4.1 Previous searches

The LEP collider established constraints on each of the eight the parameters h_i^V in the context of the process $e^+e^- \rightarrow Z\gamma$. In a statistical combination of searches performed by the DELPHI, L3, and OPAL experiments, examining 3 fb^{-1} of e^+e^- collision data for \sqrt{s} ranging from 130 GeV to 209 GeV, the 95% CL intervals of seven of the parameters contain 0, with total ranges between 0.05 and 0.10 for h_i^γ and between 0.14 and 0.25 for h_i^Z ; the 95% CL interval for the remaining factor h_4^γ spans 0.01 to 0.05 [24].

The LEP combined analysis assumed that all but one of the eight parameters were fixed to the SM expectation of 0 (i.e. these are 1D limits). It was also the last major

effort to obtain limits on $h_{1,2}^V$ independently of $h_{3,4}^V$, as subsequent searches have taken the present approach of focusing on $h_{3,4}^V$ alone, for the reasons listed above. Uniquely among the LEP experiments, the L3 Collaboration also placed limits on correlated pairs of parameters (2D limits), shown in Fig. 1.6 [11].

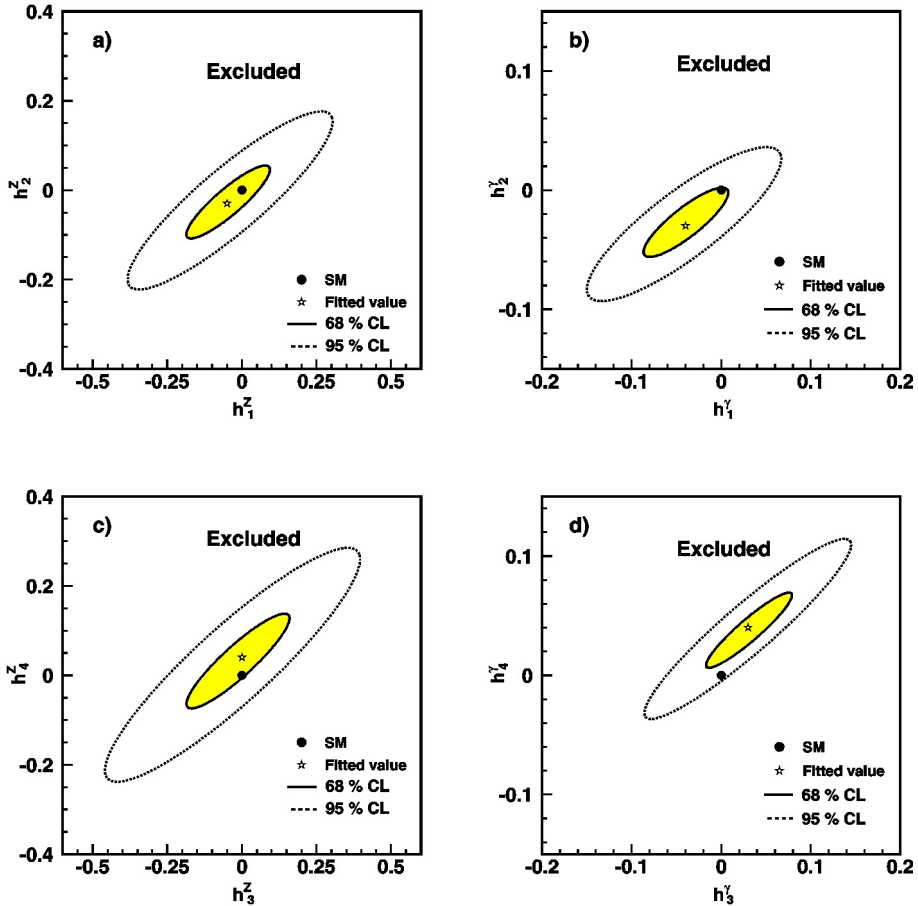


Figure 1.6: h_i^V exclusion contours from the L3 experiment at the LEP collider, as shown in [11].

Experiments at the Tevatron collider improved these limits in analyses of $p\bar{p}$ collision data at $\sqrt{s} = 1.96$ TeV. The Tevatron analyses incorporated a form factor $1/(1 + \hat{s}/\Lambda^2)^n$, by which a constant term h_{0i}^V is multiplied to obtain h_i^V . The form factor is essentially arbitrary; n is set equal to i and Λ (not to be confused with

the EFT suppression scale, below) is set to 1.5 TeV by convention. This form factor was introduced in the common reference [19] but was not used in LEP [24] or most subsequent LHC analyses, which treat the h_i^V parameters as constants independent of \hat{s} .

The CDF experiment combined analyses of $Z(\nu\bar{\nu})\gamma$ processes, using 4.9 fb^{-1} of data, and processes where the Z decays to l^+l^- (e^+e^- or $\mu^+\mu^-$), using 5.1 fb^{-1} of data. They set 95% Bayesian credibility intervals constraining $|h_3^V| < 0.022$ and $|h_4^V| < 0.0009$ (1D limits) [25]. The D0 experiment similarly combined a 3.6 fb^{-1} $Z(\nu\bar{\nu})\gamma$ analysis with a 7.2 fb^{-1} $Z(l^+l^-)\gamma$ analysis to set 95% CL limits constraining $|h_{03}^V| < 0.027$ and $|h_{04}^V| < 0.0014$ (1D limits) [26]. Correlated 2D limits were also computed and are shown in Fig. 1.7.

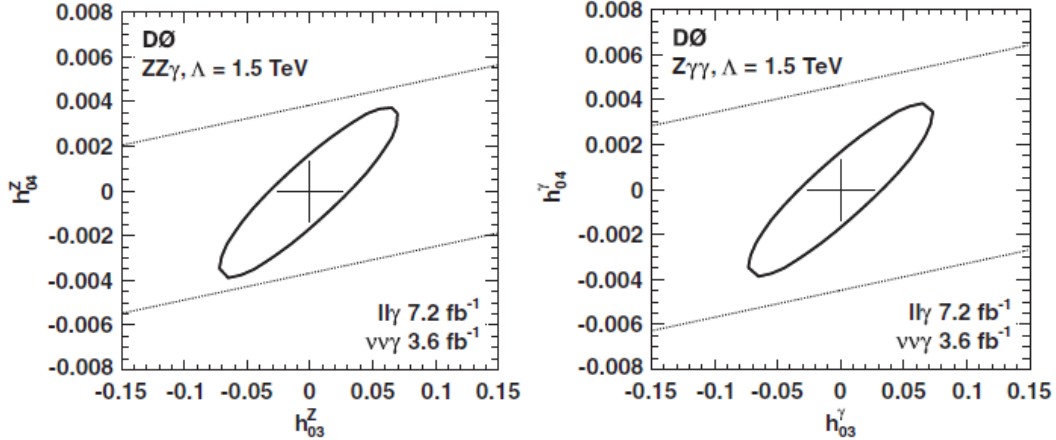


Figure 1.7: h_{0i}^V exclusion contours from the D0 experiment at the Tevatron collider, from [26].

Experiments at the LHC made further improvements via the analysis of pp collision data at progressively higher \sqrt{s} . A summary of 1D limits on h_i^V from both the ATLAS and CMS experiments obtained from analyses of $\sim 20 \text{ fb}^{-1}$ of $\sqrt{s} = 8 \text{ TeV}$ data is shown in Fig. 1.8. ATLAS limits show the results of combined $Z(\nu\bar{\nu})\gamma$ and $Z(l^+l^-)\gamma$ analyses, both with and without a form factor on h_i^V . CMS limits show

separate $Z(\nu\bar{\nu})\gamma$ results, along with $Z(l^+l^-)\gamma$ results, both without a form factor [23].

These comparisons make clear that $Z(\nu\bar{\nu})\gamma$ is by far the more sensitive channel for setting aTGC limits.

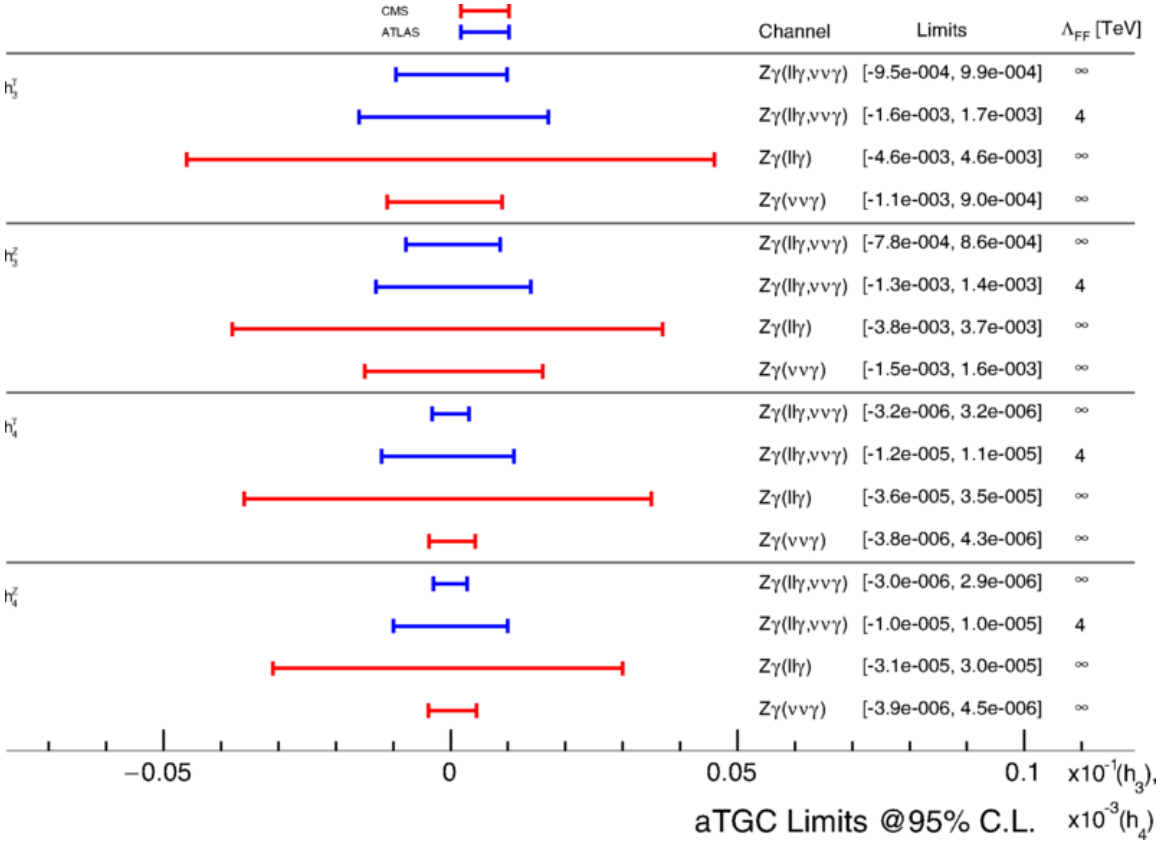


Figure 1.8: 1D h_i^V exclusion limits from the ATLAS and CMS experiments at the LHC based on 20 fb^{-1} of $\sqrt{s} = 8 \text{ TeV}$ pp collision data, from [23]. $Z\gamma(l\gamma)$ indicates a combination of $Z(e^+e^-)\gamma$ and $Z(\mu^+\mu^-)\gamma$ analyses; $Z\gamma(l\gamma, \nu\nu\gamma)$ indicates a combination of these with $Z(\nu\bar{\nu})\gamma$. The mass Λ_{FF} is the form factor scale; ∞ means no form factor was used.

The most sensitive published limits on $h_{3,4}^{Z,\gamma}$ are currently derived from 36.1 fb^{-1} of 13 TeV pp collision data collected by the ATLAS detector at the LHC, analyzed exclusively in the monophoton channel, with no form factor [15]. These are summarized in Figs. 1.9, 1.10.

None of these analyses report any significant evidence of BSM physics.

Parameter	Limit 95% C.L.	
	Measured	Expected
h_3^γ	$(-3.7 \times 10^{-4}, 3.7 \times 10^{-4})$	$(-4.2 \times 10^{-4}, 4.3 \times 10^{-4})$
h_3^Z	$(-3.2 \times 10^{-4}, 3.3 \times 10^{-4})$	$(-3.8 \times 10^{-4}, 3.8 \times 10^{-4})$
h_4^γ	$(-4.4 \times 10^{-7}, 4.3 \times 10^{-7})$	$(-5.1 \times 10^{-7}, 5.0 \times 10^{-7})$
h_4^Z	$(-4.5 \times 10^{-7}, 4.4 \times 10^{-7})$	$(-5.3 \times 10^{-7}, 5.1 \times 10^{-7})$

Figure 1.9: 1D h_i^V exclusion limits from the ATLAS experiment at the LHC based on 36.1 fb^{-1} of $\sqrt{s} = 13 \text{ TeV}$ pp collision data, analyzed in the monophoton channel, as shown in [15].

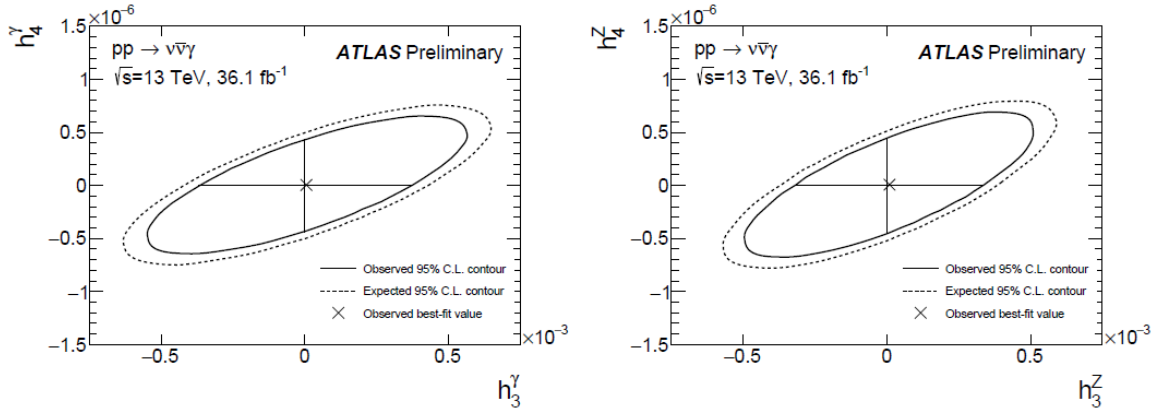


Figure 1.10: 2D h_i^V exclusion contours from the ATLAS experiment at the LHC based on 36.1 fb^{-1} of $\sqrt{s} = 13 \text{ TeV}$ pp collision data, analyzed in the monophoton channel, as shown in [15].

1.5 Dark matter EFT and simplified models

The standard theory of gravitation, Einstein's general theory of relativity (GR), has passed experimental tests over scales ranging from the orbits of satellites [27] to the entire observable universe [28], matching observations more closely than Newton's theory of gravitation, to which it converges in the weak-field limit [29]. It predicts the existence of gravitational waves, directly detected for the first time in 2015 [30],

and these have been used to test the theory in the strong-field regime [31].

Despite its many triumphs, GR fails—under the assumption that SM particles and their known interactions are the only sort that exist—to describe the orbits of stars in nearly every galaxy [32], the average weak distortion of light by galaxies [33], the strong distortion of light by galaxy clusters [34], the orbits of galaxies in galaxy clusters [35], the formation of large-scale filamentary structures [36], or the distribution of ripples in the cosmic microwave background (CMB) arising from big bang nucleosynthesis [28]. Each of these phenomena could be explained by the existence of an abundance of massive matter with no discernible interactions of any sort, other than gravitation. This extends to interactions with visible light, giving rise to the name “dark matter.”

These difficulties could also indicate the need to modify the theory of gravity. However, the nature of the Bullet cluster, a galaxy cluster with a center of mass displaced from its visible mass center, is challenging to explain in a theory of gravity without DM that can also explain all of the preceding observations. In contrast, it has a straightforward explanation if GR+DM is true: the displaced mass is DM [37]. Furthermore, if a modified theory of gravity results in the apparent gravitational effect of DM on galactic scales, then the existence of a galaxy without any apparent DM, as observed in [32], is also challenging to explain. It’s conceivable that a random collection of stars could agglomerate into a galaxy without the assistance of DM, or else become separated from their DM component (as with the Bullet cluster), but the fundamental laws of gravitation should not fail in just one galaxy.

No SM particle is predicted to exhibit the behavior of DM, and this has spurred the development of BSM theories describing new particles that could account for it [38–41]. The great diversity of theories motivates general models that can potentially constrain a wide variety of specific theories simultaneously. If DM is particulate

in nature, it apparently has a substantial mass, interacts very weakly with SM particles, and is stable on cosmological timescales []. The models we consider here include a BSM particle satisfying each of these criteria. All the massive, stable particles in the SM are fermionic, and these models similarly describe a fermionic DM candidate. Otherwise, the new physics content of these models is kept to a minimum, as sufficiently large deviations from SM predictions would presumably have been detected by now.

One model we examine describes a direct coupling between DM and the neutral EWK vector bosons Z and γ [42]. The model does not fully specify the nature of the proposed particle and its SM interactions, but rather only predicts the most dominant potential signature of new physics, by adding a handful of new operator terms to the SM Lagrangian. Any operator has a *mass dimension*, denoted in powers of GeV. The SM Lagrangian has a mass dimension of 4, and any operator term added to it has to have this same mass dimension for the expression to be coherent. Additional particle interactions in an operator term tend to raise the mass dimension. If an operator describes an especially intricate interaction, the overall term must be multiplied by an extra factor of $(\frac{1}{\Lambda})^n$ to maintain an overall mass dimension of 4, where Λ is some mass scale in GeV and n is a positive number.

Operator terms with nonzero powers of $\frac{1}{\Lambda}$ tend to have their interactions suppressed for interaction energies much smaller than Λ , and so Λ is called the *suppression scale*. The effects of more complicated terms, multiplied by higher powers of $\frac{1}{\Lambda}$, are expected to become apparent at higher interaction energy scales, so a model that only incorporates simpler terms is expected to lose predictive validity as the interaction energy approaches Λ [43]. A model that only adds a restricted set of terms, with predictive validity only up to energies below Λ , is called an EFT.

The DM-EWK EFT described in [42] adds four dimension-7 interaction terms

to the SM Lagrangian, which therefore carry factors of $\frac{1}{\Lambda}$ raised to the third power. The mass m_{DM} of the new DM particle is a free parameter of the model, along with two constants k_1 and k_2 controlling the relative strengths of the DM- Z and DM- γ couplings. Fig. 1.11 illustrates the dominant contribution of this interaction to monophoton yields. Since the DM particle only interacts with the Z and γ , and this interaction is suppressed by $(\frac{1}{\Lambda})^3$, the outgoing DM is not expected to interact with any detector elements.

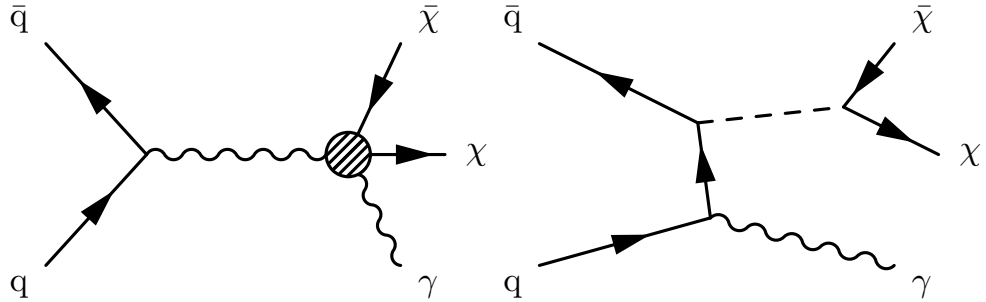


Figure 1.11: Leading order Feynman diagrams for monophoton processes in a DM-EWK EFT (left) and in DM simplified models (right). The intermediate boson in the EFT diagram can be a Z or γ . The dotted line in the DM simplified model diagram stands for the DM-quark mediator.

Since the DM pair emerges directly from an EWK boson, this EFT is limited in the dynamics it can describe. In contrast, so-called *simplified models* of DM add a new mediating boson between the DM and SM fermions [44], which more typically characterizes the fermion interactions that we know from the SM. These models are still “simplified” in that they fall short of a complete theory of particle physics valid in all contexts—for example, the DM lacks a coupling to the H , but still has mass. Nevertheless, some kind of DM–mediator–SM interaction is a generic feature of many new physics models, and so limits on the strength of this interaction potentially constrain a broad class of more specific models.

We examine models in which the mediator has either exclusively vector or exclu-

sively axial-vector couplings to DM and also to SM quarks, independently of quark flavor. The free parameters of this model include the DM mass m_{DM} , the mediator mass M_{med} , the DM-mediator coupling g_{DM} and the DM-quark coupling g_q . The leading Feynman diagrams for monophoton production are shown in Fig. 1.11. The mediators are typically chosen to be quite massive, which suppresses the likelihood of DM-quark interactions, and the mediator does not have any direct couplings to leptons or bosons, so the DM is not expected to interact with detector elements as it escapes.

1.5.1 Previous searches

In the limit that M_{med} is much larger than the $q\bar{q}$ interaction energy, DM simplified models converge to an EFT describing a direct contact interaction between DM and quarks, with a suppression scale $M_* = M_{\text{med}}/\sqrt{g_q g_{\text{DM}}}$ [45]. Such DM-quark EFT models were the subject of monophoton searches [46, 47] prior to the adoption of DM simplified models by the ATLAS-CMS Dark Matter Forum in 2015 [44]. As the interaction energy increases, the EFT description breaks down for the reasons described above, and DM simplified models offer a replacement that retains predictive validity (at the cost of some degree of generality). In contrast, the dimension-7 DM-EWK EFT considered here is not the large- M_{med} limit of a DM simplified model [44] and represents a truly distinct process topology.

Both the DM simplified models and the DM-EWK EFT were developed after LHC data taking began, with comparisons to LHC data in mind [42, 44]. Thus, the history of examination of these models begins with analyses of data collected by the ATLAS and CMS experiments at the LHC. In general, limits on BSM models set by LHC experiments become stronger at higher energies and with larger data sets. The remainder of this section describes the most stringent experimental limits set by the

ATLAS and CMS experiments, each based on analyses of 13 TeV pp collision data collected in 2016.

New physics introduced by DM simplified models is expected to contribute to a variety of other signatures in addition to the monophoton signature. Figure 1.12 compares analyses in three different “mono-X” channels based on data collected by the CMS detector, including the most recent monophoton results described herein. Each of the three searches examine similar final state characteristics; they are primarily distinguished by the type of particle(s) emerging against the \vec{p}_T^{miss} , listed in the caption. The limits on DM simplified model parameters set by the monophoton search are generally more stringent than those set by mono- Z search, but less stringent than those set by the mono- j/V search. The concordance of results from each of these three independent analyses reinforces the degree of confidence with which model parameters are excluded, and in the event of a new physics discovery in one channel, the nature of the discovery will be further illuminated by searching for a corroborating signature in other channels.

Prior to the analysis presented in this thesis, the last published results from CMS in the monophoton final state examined 12.9 fb^{-1} of data collected in the first half of 2016 [52]. Simplified models were excluded at 95% CL for M_{med} up to 700 GeV at small values of m_{DM} , in both the vector and axial-vector cases. Values of Λ for the DM-EWK EFT up to 600 GeV were also excluded at 95% CL, assuming $k_1 = k_2 = 1$ ³.

The most stringent monophoton results to date are set by an analysis of 36.1 fb^{-1} of data collected by the ATLAS detector [53]. Simplified models were excluded at 95% CL for M_{med} up to 1200 GeV at small values of m_{DM} , in both the vector and axial-vector cases, as shown in Fig. 1.13. Values of Λ for the DM-EWK EFT up to

³Defining $k = \sqrt{k_1^2 + k_2^2}$ and $\theta_k = \arctan \frac{k_2}{k_1}$, the choice $k_1 = k_2 = 1$ corresponds to the choice $k = \sqrt{2}$ and $\theta_k = \pi/4$. Fixing $\theta_k = \pi/4$, the limits on $\Lambda/k^{1/3}$ for arbitrary k are equal to the $k = \sqrt{2}$ limits on Λ multiplied by $2^{-1/6}$.

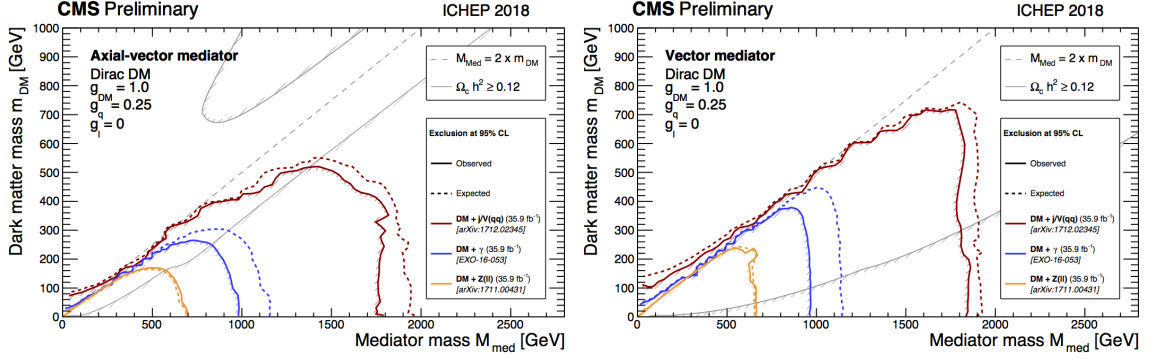


Figure 1.12: Summary plots of limits on DM simplified model parameters, shown in [48]. Simplified models are excluded at 95% CL or above for parameter values under the contours. Results based on three different final states are shown: mono- $Z(l)$ [49] in yellow, mono- $j/V(qq)$ [50] in red, and monophoton [51] in blue, the latter corresponding to the new results presented in this thesis. The Ω_c^2 curves correspond to constraints on the cosmological DM abundance set by Planck satellite measurements [28].

790 GeV, assuming $k_1 = k_2 = 1$, were also excluded at 95% CL, as shown in Fig. 1.14.

Assuming DM simplified models describe the dominant mode of interaction between DM and SM particles, the scattering cross section of low-energy (nonrelativistic) DM off nucleons (protons and neutrons) is uniquely determined [45]. This allows DM simplified model limits to be compared directly with limits set by *direct detection* (DD) experiments, which search for freely-floating ambient DM by looking for signatures of DM scattering off of target nuclei. The most recent ATLAS results are plotted against a variety of DD limits in Fig. 1.15. An axial-vector/vector mediator corresponds to a DM-nucleus cross section that does/does not depend on the spin of the nucleus, respectively known as the spin-dependent/spin-independent (SD/SI) cross section.

All of the preceding limits were derived for $g_{\text{DM}} = 1$ and $g_q = 0.25$, which matches the couplings used for the results obtained herein. By convention, this is the most commonly investigated set of values for these couplings, but studies have been done

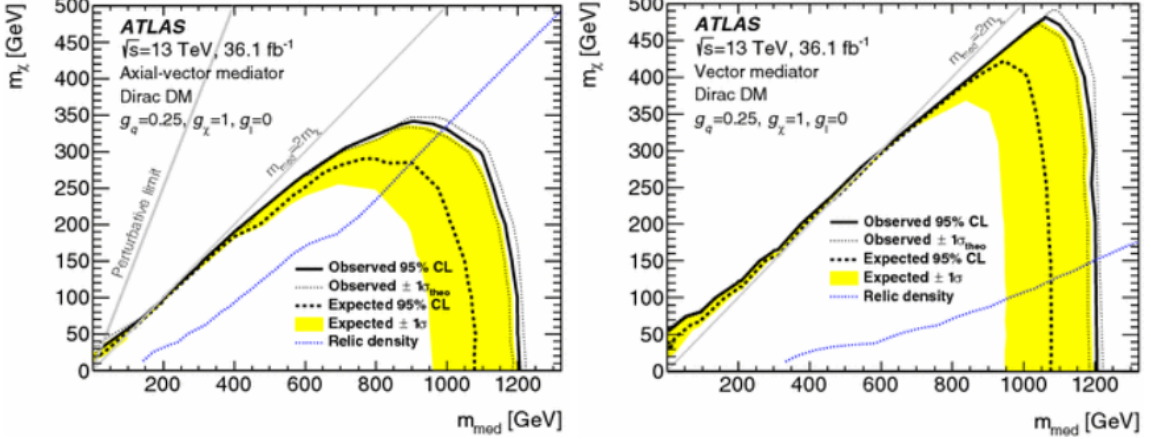


Figure 1.13: Limits on DM simplified model parameters set by the ATLAS experiment, as shown in [53]. Simplified models are excluded at 95% CL or above for parameter values under the contours. The relic density curves correspond to constraints on the cosmological DM abundance set by Planck satellite measurements [28].

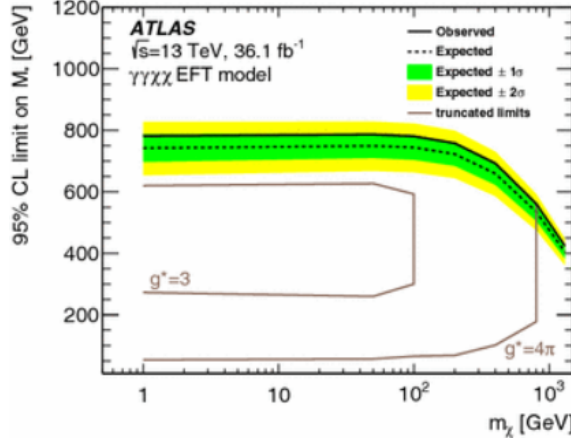


Figure 1.14: Limits on the DM-EWK EFT set by the ATLAS experiment, as shown in [53]. The DM-EWK EFT is excluded at 95% CL or above for values of Λ under the contour.

using alternative values, some of which include a small nonzero coupling between the new mediator and charged leptons (e.g. [53]).

None of these analyses report any significant evidence of BSM physics.

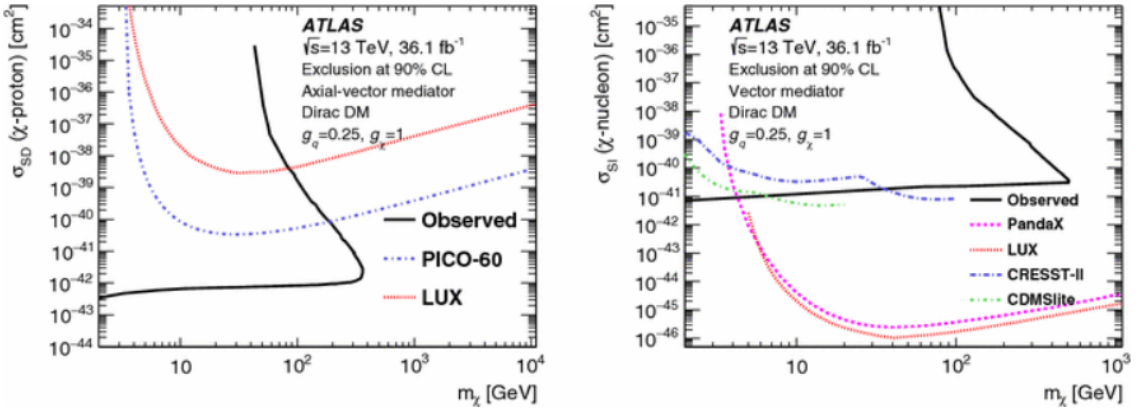


Figure 1.15: Limits on low-energy DM-nucleon scattering cross sections set by the ATLAS experiment, as shown in [53]. The ATLAS limits are compared against limits on the SD cross section from PICO-60 [54] and LUX [55] (left) and limits on the SI cross section from PandaX-II [56], LUX [57], CRESST-II [58], and CDMSlite [59] (right). Scattering cross sections are excluded at 90% CL or more above the contours.

1.6 ADD gravitons

We finally examine a model of gravitation in extra dimensions originally proposed by Arkani-Hamed, Dimopoulos, and Dvali (ADD) [60]. Gravity typically affects SM particles much, much less than the other fundamental interactions. The weakness of gravity is often expressed in terms of a fundamental mass scale M_{Pl} ($\sim 10^{19}$ GeV), which is many orders of magnitude larger than the masses of the EWK bosons ($\sim 10^2$ GeV). Particle-level gravitational interactions are correspondingly sharply suppressed. The proposed boson of gravitation, the graviton, has yet to be detected and is not part of the SM. The mystery of why M_{Pl} is so much larger than the EWK mass scale has been called the “Hierarchy problem,” and the desire for a more elegant formulation has been a productive stimulus for BSM theories [60, 61].

Everyday experience indicates that there are 3 dimensions of space and 1 dimension of time, and the SM assumes this to be true. The ADD model begins with the observation that, if there are n extra spatial dimensions beyond the usual 3, we

might not be able to directly perceive them if all the SM particles are confined by some as-yet-unspecified mechanism to a 3+1-dimensional subspace (the “brane”) of the full $n+3+1$ -dimensional spacetime (the “bulk”)⁴. In contrast, gravitons in this model are able to propagate freely throughout the bulk.

Gravitation in the bulk is characterized by a mass scale M_D distinct from the mass scale M_{Pl} that characterizes gravitation as perceived by particles confined to the brane. If the extra dimensions are not extended infinitely like the dimensions of common experience, but rather “compactified” into a finite volume of characteristic radius R , then for a sufficiently mild energy density in the vicinity of the brane, $M_{\text{Pl}}^2 \approx M_D^{n+2} R^n$ [60, 62]. For a modest number of extra dimensions (e.g. $3 \leq n \leq 6$), the observed large value of M_{Pl} could then really be a consequence of a large value for R , while the fundamental gravitational scale M_D could be closer to or even the same as the EWK scale. In light of this possibility, ADD model predictions are typically examined for values of M_D in the vicinity of 1 TeV.

The cross sections for a variety of graviton production scenarios are calculated in ref. [62], using a low-energy EFT approximation of GR in which M_D serves as the suppression scale. At higher energies the specific details of the geometry of the extra dimensions, and phenomena uniquely predicted by a full quantum theory of gravitation, would start to become apparent. These are both unknown, and the EFT correspondingly does not make predictions on the outcome of scattering events with energies above M_D .

The ratio M_{Pl}/M_D essentially expresses the wide range of kinematic possibilities that open up for gravitons with the addition of extra dimensions. After summing over all of these possibilities, the resulting cross section is high enough for graviton production to be probed with existing collider experiments. Gravitons couple to every

⁴The case $n = 0$ corresponds to ordinary GR.

SM particle, although the coupling is still sufficiently weak that an emitted graviton will generally not interact with a detector element. This results in a monophoton signature if it is emitted opposite a photon, as illustrated in Fig. 1.16.

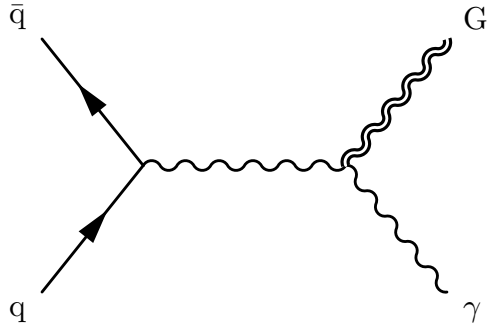


Figure 1.16: Diagram illustrating ADD graviton emission resulting in a monophoton signature.

1.6.1 Previous searches

For distances r much larger than R , the effective gravitational potential in the ADD model has the $1/r$ form proposed by Isaac Newton (in the weak-field limit). However, for $r \ll R$, the Newton's law potential is multiplied by $(R/r)^n$, leading to significant deviations from Newtonian gravitational behavior. If $M_D \approx 1 \text{ TeV}$ and $n = 1$, then to reproduce the observed value of M_{Pl} , R must be $\sim 10^{13} \text{ cm}$, which would result in noticeable differences in the orbits of the planets [60]. The case $n = 2$ is disfavored by precision measurements of Newton's law over distances on the order of 0.1 mm [61].

As in the case of the aTGC model, collider limits become strictly more stringent with increases in collider energy, starting from the LEP and moving up through the Tevatron to the LHC. Representative curves from each of these are shown in Fig. 1.17, which also shows that collider limits on M_D dominate noncollider limits for $n \geq 3$.

Prior to the analysis presented in this thesis, the most stringent ADD limits in

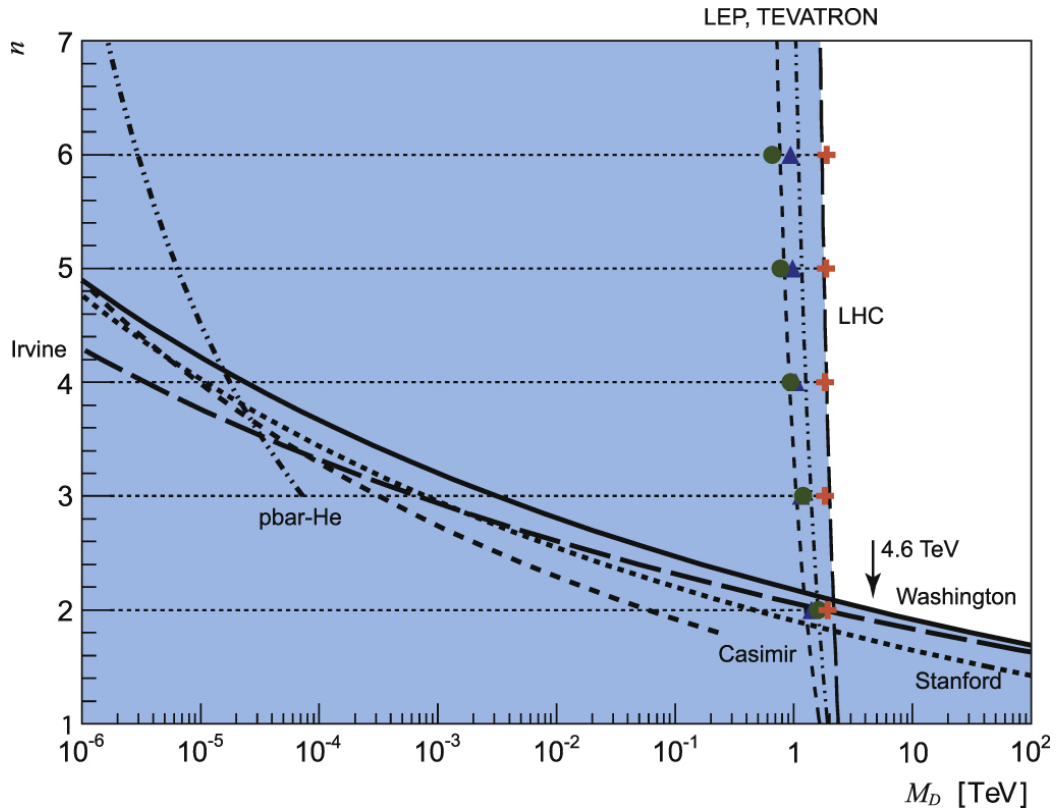


Figure 1.17: Comparison of collider and noncollider limits on ADD model parameters, as shown in [61]. The marked points are monojet limits from the LEP [63], Tevatron [64], and LHC [61, 65, 66]. The Irvine [67, 68], Washington [69], and Stanford [70] curves come from direct measurements of Newton's law. The Casimir curve [61] synthesizes of a range of experimental results that constrain the existence of strong gravity using the Casimir force, and the pbar-HE curve [61, 71] comes from analyses of electron double scattering and exotic atom spectroscopy. The ADD model is excluded at 95% CL or more in the shaded region.

the monophoton final state were set in the last published results from CMS, based on 12.9 fb^{-1} of data collected in the first half of 2016 [52]. The ADD model was excluded at 95% CL for M_D up to 2.31 TeV for $n = 3$, climbing to 2.49 TeV at $n = 6$, as shown in Fig. 1.18.

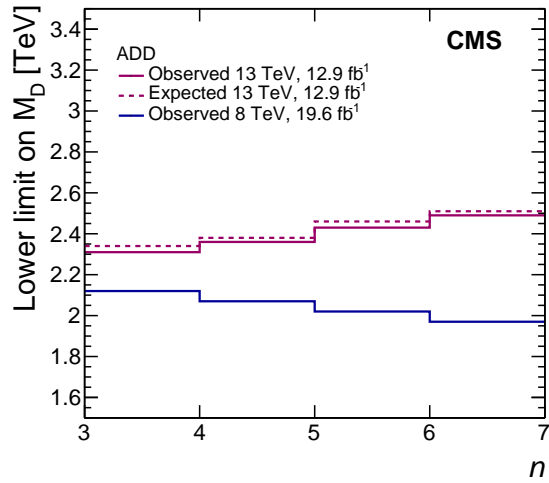


Figure 1.18: ADD limits set by the CMS experiment using data from the first half of 2016, as shown in [52]. Limits from the previous CMS analysis of 8 TeV data [46] are also shown. The ADD model for a given n (specified by the left edge of each bin) is excluded at 95% CL or more for M_D below the curves.

None of these analyses report any significant evidence of BSM physics.

Chapter 2

The CMS experiment and the LHC

2.1 The LHC

The Large Hadron Collider (LHC) [72] at CERN is, as the name suggests, the world’s largest and most powerful particle accelerator. It is used to collide protons as well as heavy ions, which are both examples of hadrons, hence the “HC” in LHC. Experiments attached to the collider examine the collision debris, from which features of the parent hard-scattering process may be inferred, allowing models such as those described in Chap. 1 to be tested.

The collider consists of a closed loop of beam pipes, along with its RF cavities (sec. 2.1.1), magnets, and cryogenic and vacuum systems. It sits in a circular tunnel 26.7 km in circumference, lying between 45 and 170 m underground, straddling the French–Swiss border near Geneva, Switzerland. The beam pipes are subdivided into eight straight and eight arc sections, forming a rounded octagon. To orient navigation, there are eight designated points spaced evenly around the tunnel perimeter, one in the middle of each 8528 m-long straight section. The four main LHC experiments surround the LHC beam pipe at four of these points: ATLAS [73] at point

1, ALICE [74] at point 2, CMS [75] at point 5, and LHCb [76] at point 8. Their arrangement is shown in Fig. 2.1.

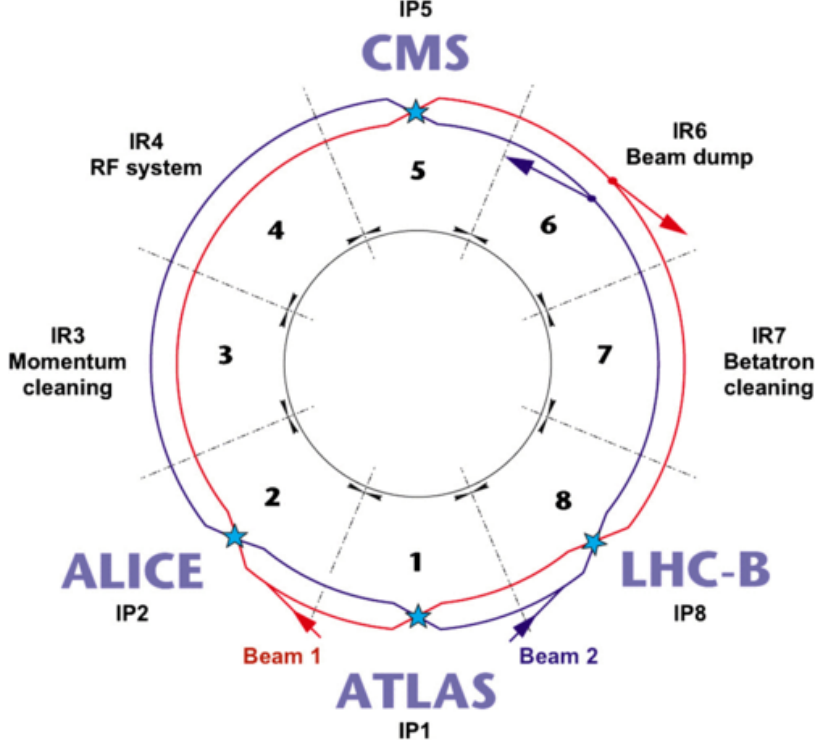


Figure 2.1: Schematic layout of the LHC, from [77].

The eight arc sections each have a radius of curvature $R = 2.804 \text{ km}$. This radius is constrained by the energy of a relativistic particle bent in a circular trajectory by a magnetic field of magnitude B , via the relation [78]

$$E = qcBR \quad (2.1)$$

where q is the particle's electric charge and c is the speed of light. For a fixed particle type and magnet strength, E is directly proportional to R . Accordingly, higher-energy colliders tend to be built with larger circumferences than lower-energy colliders. The energy of a fully-accelerated LHC proton in 2016 was 6.5 TeV, corresponding to a bending magnet strength of 7.7 T.

Smaller accelerators including the Proton Synchrotron (PS) and Super Proton Synchrotron (SPS) used to be flagship accelerators in their own right, but now chiefly serve as intermediate stages in an accelerator complex that feeds the LHC. The LHC itself occupies the tunnel originally dug to house the Large Electron-Positron (LEP) collider [79], which collided electrons and their antipartners (positrons) and ran from 1989 until 2000, setting some of the original results listed in Chap. 1. The Fermilab Tevatron [80], which ran from 1983 to 2011, occupied a smaller tunnel but achieved higher energies than LEP by accelerating heavier particles: protons and their antipartners¹. The LHC, inaugurated in 2008, accelerates protons in the world’s largest accelerator tunnel, with state-of-the-art bending magnets, allowing it to achieve unprecedented particle collision energies.

2.1.1 Proton acceleration and collision

The substantial circumference of the LHC beam pipe is compensated by a somewhat narrow width. In practice, a low-energy beam is too wide to inject directly into the LHC, but the beam can be narrowed by accelerating it. Furthermore, the beam energy in a specific accelerator of radius R can be tuned by adjusting B , but due to the restricted range of accessible B values for any given magnet [78], a single accelerator can only accommodate a restricted beam energy range. The beam is therefore passed through multiple accelerators of increasing size before ultimately arriving at the LHC, each of which increases its energy by an amount commensurate with its radius. Protons are initially collected by ionizing hydrogen gas and then fed to the LINAC2, a linear accelerator, which accelerates them to 50 MeV before sending them to the PS booster, which brings them up to 1.4 GeV. The protons are then sent to the PS, taking them to 25 GeV, and after that to the SPS, which pushes

¹These and other recent collider experiments are reviewed in [6], chapter 30.

them to 450 GeV before finally injecting them into the LHC for final acceleration up to 6.5 TeV.

Protons are accelerated by passing through radio-frequency (RF) cavities, which generate oscillating electromagnetic fields. Forward acceleration only results if the proton passes through the RF cavity at an opportune point in its oscillation cycle. Thus, rather than circulating in a continuous beam, protons are segregated into discrete *bunches*. In the LHC, the RF frequency is tuned to 400.790 MHz, and bunches are spaced so as to keep 10 RF oscillations between each bunch. This corresponds to a minimum bunch separation of 24.95 ns in time, with enough length in the tunnel to fit exactly 3564 bunches, each orbiting with a frequency $f_{\text{rev}} = 11.245 \text{ kHz}$. A maximum of 2808 bunches can be injected in practice, to allow a sufficiently long empty interval for the beam injection and beam dump redirector magnets to activate, and also respecting constraints imposed by assembling the bunch trains via the accelerator chain. Beam optimization strategies and other operational constraints, including a persistent vacuum leak in the SPS beam dump during 2016, can reduce this further. In 2016, the typical number of bunches per beam n_b was 2076.

Two separate bunch trains counter-rotate around the LHC in separate beam pipes, with their paths crossing at four collision points corresponding to each of the main experiments. The center-of-mass collision energy of the beams, \sqrt{s} , is twice that of the individual beam energies. For a single-beam energy of 6.5 TeV, this corresponds to $\sqrt{s} = 13 \text{ TeV}$. Each bunch contains many billions of protons: in 2016, the typical number of protons per bunch at the start of each fill, N_b , was 1.25×10^{11} . As a consequence, many pairs of protons can undergo hard collisions within the same bunch crossing, depending on the instantaneous luminosity \mathcal{L} and the total inelastic pp scattering cross section σ_{inel} . In 2016, there were on average 23 of these *pileup* collisions per bunch crossing.

Normalized transverse emittance ϵ_n	3.4 μm
β^*	40 cm
Crossing angle θ_c	185 μrad
RMS longitudinal bunch length σ_z	7.87 cm

Table 2.1: Beam geometry parameters for 2016

Various parameters describing the geometric profile of the bunches are listed in Table 2.1. These determine \mathcal{L} at the collision points, via

$$\mathcal{L} = \frac{N_b^2 n_b f_{\text{rev}} \gamma_r}{4\pi \epsilon_n \beta^*} \left(1 + \frac{\theta_c^2 \sigma_z^2 \gamma_r}{4\epsilon_n \beta^*} \right)^{-1/2} \quad (2.2)$$

in which the relativistic factor $\gamma_r = E_{\text{beam}}/m_p$ has a value of 6930 for $E_{\text{beam}} = 6.5 \text{ TeV}$. The value of \mathcal{L} corresponding to the typical 2016 parameter values listed above is $1.3 \times 10^{34} \text{ cm}^{-2}\text{s}^{-1}$.

2.1.2 Collimation, magnets, and beam halo

The beams can lose protons during transit through a variety of mechanisms, such as intra-beam scattering and scattering off of residual gas inside the tunnel [72]. Among other consequences, this leads to the accumulation of a “halo” of protons with large radial separation from the central beam axis, accompanying the main beam. If left unchecked, beam halo could damage unprotected equipment and leave spurious signals in detectors. Furthermore, if a bending magnet were to suddenly fail, the beam would sweep across the area downstream of the magnet, dumping a potentially devastating load of radiation on whatever it hit.

Collimators stationed around the beam line capture and remove this halo, and additionally protect the LHC and its detectors from sudden beam control failure. Every proton–collimator interaction produces a residual shower of secondary particles that emerge from the other side of the collimator and continue forward, so a series of several collimators is required. Primary LHC collimators (TCP) clean the beam

at Points 3 and 7, and secondary collimators (TCS) catch most of the output from those. Tertiary collimators (TCT) made of a heavy tungsten alloy sit on either side of the CMS experimental cavern, to scrub as much remaining halo as possible before it reaches the detector [77].

As noted above, a charged particle has its trajectory bent as it moves through a magnetic field, and this principle is used to guide the beams. A series of 1232 main dipole magnets spaced around the LHC, mostly in the arc regions, keep the beams moving in their quasi-circular trajectories around the tunnel. A multitude of other magnets serve more specialized roles. Quadrupole magnets have the effect of squeezing the beam along one axis and stretching it along another, and are used to focus the beam along a specific direction. Near the interaction point (IP) of each experiment, an inner triplet of quadrupole magnets are the last to interact with the beams before they collide. Figure 2.2 shows the arrangement of magnets near the ATLAS and CMS IPs.

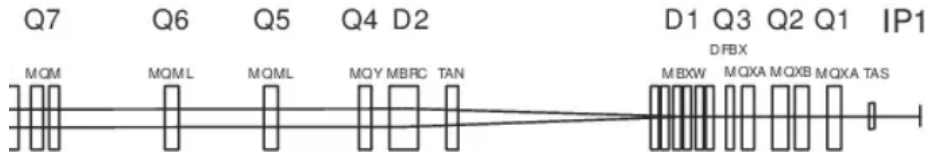


Figure 2.2: Dipole (D1-2) and quadrupole (Q1-7) magnet arrangement near the left side of the IP, from [81]. This arrangement is mirrored on the right side of the IP. The figure specifically designates IP1, the ATLAS IP; the magnet layout is identical around IP5, the CMS IP. The inner triplet of quadrupole magnets (with two varieties, designated MQXA and MQXB) are the last to interact with the beam before collision. The distance from the left edge of Q3 (MQXA) to the IP is about 53 m, and the distance from the right edge of Q1 to the IP is about 23 m. The TCT sits between D2 and TAN, about 150 m from the IP.

The envelope of each beam reaches a maximum in the inner triplet before finally being focused toward a minimum at the interaction point. Beam halo is correspondingly widely dispersed, and the TCTs are specifically placed about 150 m out from

the IP so as to protect the inner triplet from this halo [82]. Secondary particles produced from beam halo collisions with the TCTs include large numbers of high-energy muons, along with an assortment of other secondaries. These, along with the secondaries from proton collisions with residual gas in the beam pipe, comprise what is called the machine-induced background (MIB) impinging on CMS [83].

In contrast to protons in the beam, secondary muons are neither narrowly nor evenly focused by the final stretch of magnets before reaching the IP. They enter the CMS cavern traveling parallel to the beam pipe with a wide radial profile, often having a high enough radius to hit the exterior muon chambers and calorimeters [83]. Furthermore, the transverse distribution of MIB (Fig. 2.3) is highly anisotropic, concentrating near the horizontal plane.

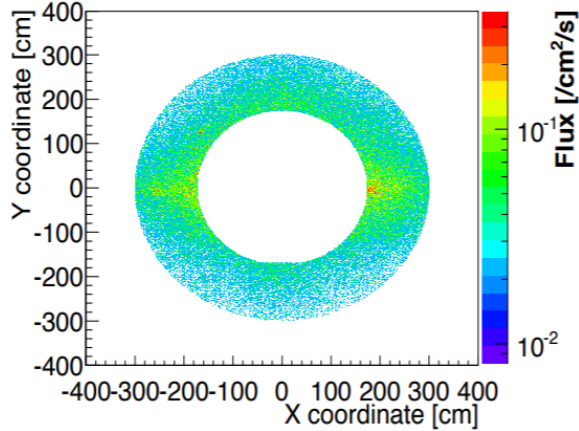


Figure 2.3: Simulated distribution of MIB flux transverse to the beam pipe in the CMS cavern, 20.6 m from IP5. From [83]. The x and y coordinates are defined in sec. 2.2.1.

2.2 The CMS experiment

The CMS, short for Compact Muon Solenoid, is a general-purpose particle detector surrounding the LHC beam pipe centered at IP5, located 100 m underground near

Cessy, France. Multiple layers of metal absorbers, crystal and plastic scintillators, and electrically-tensed gas chambers and silicon semiconductors are arranged so as to interact with different types of particles in discernably different ways. Millions of sensors collect fine-grained information on the interactions of particles within these layers, and the resulting data is used to precisely reconstruct the type, charge, energy, momentum, and trajectory of nearly every final-state particle emerging from a hard collision event.

A broad overview of the experiment is shown in Fig. 2.4. A more comprehensive description is given in [75], the reference from which much of the material in this section derives. The CMS is a dynamically-evolving apparatus, responding to changing experimental conditions and advances in detection technology and methods. The description of CMS given in this section specifically applies to its setup in 2016, the year in which collision data for this thesis was taken.

2.2.1 Coordinate system

The coordinate system is centered at IP5, the nominal interaction point inside the CMS experiment. The positive x -direction points radially inward toward the center of the LHC ring, the positive y -direction points vertically upward, and the positive z -direction is oriented counterclockwise around the LHC when viewed from above, as in Fig. 2.5. The radial coordinate in the x – y plane is denoted r , and the azimuthal angle ϕ is measured counterclockwise (viewed from the positive z -direction, looking toward the negative z -direction) from the x -axis in this plane. The polar angle θ is measured from the positive z -direction.

The *longitudinal momentum* of a particle is defined as the component of its momentum along the z -axis, with magnitude p_L . The *transverse momentum* of a particle is the component of its momentum perpendicular to the longitudinal momentum, ly-

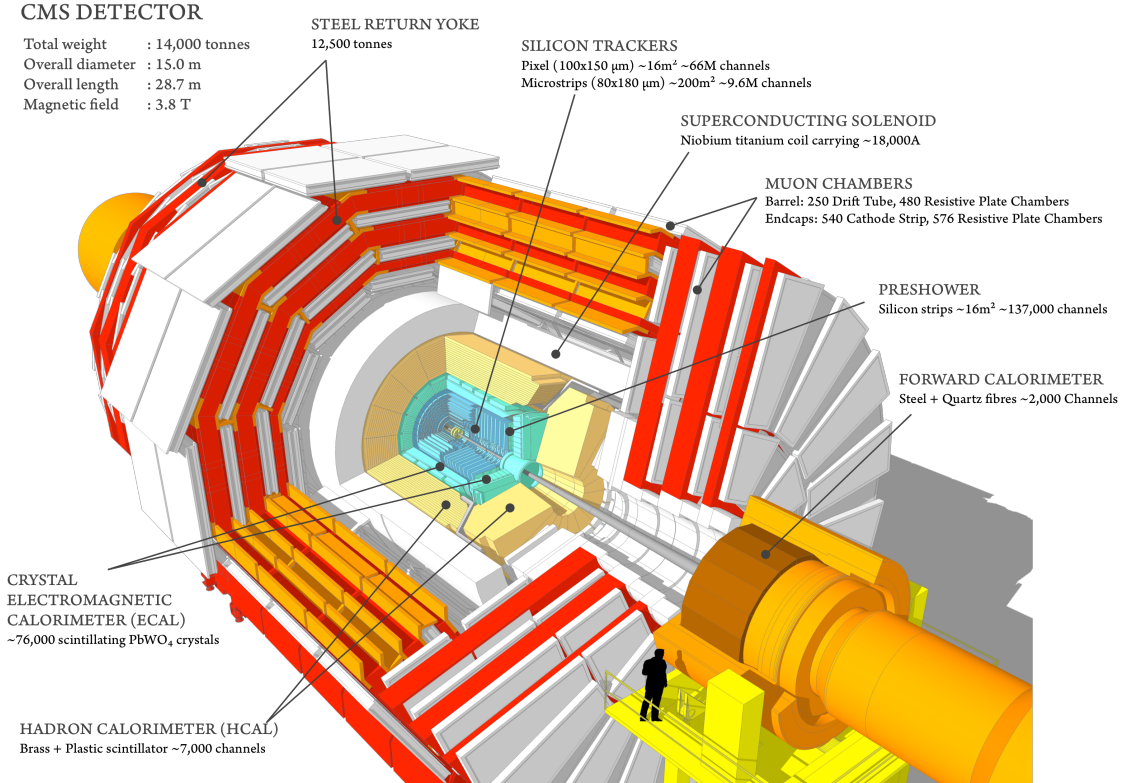
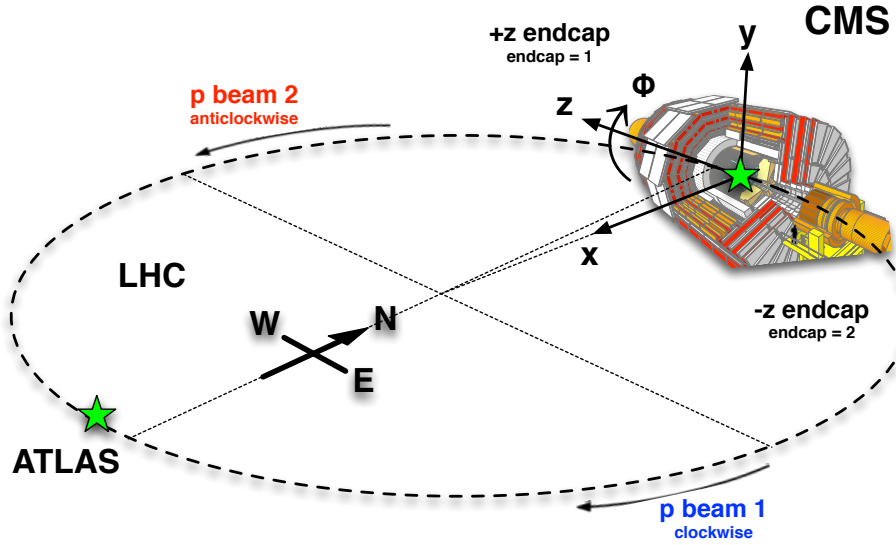


Figure 2.4: A schematic illustration of the CMS experiment, with one octant cut away for visibility.

ing in the $x-y$ plane, and can be specified by its magnitude p_T and its direction ϕ .

Hard pp collisions result in the interaction of individual partons, each of which can carry different fractions of their parent p momentum. Even if the longitudinal momenta of the colliding protons are perfectly matched, the longitudinal momenta of the interacting partons may not be. However, the p_T of both parent protons is negligible, and any fraction of zero is still zero. There is some small p_T spread of partons within a proton, but in general, the p_T of colliding partons is almost exactly zero, within the limits of detector sensitivity.

By the law of conservation of momentum, the vector sum of the transverse mo-



References: Tim.Cox@cern.ch 21.03.2013
LHC: <http://www.lhcportal.com/Portal/Info/LHCGlossaryDef.pdf>
CMS figure: <https://twiki.cern.ch/twiki/bin/view/CMSPublic/SketchUpCMS>

Figure 2.5: The CMS coordinate system.

menta of all collision products must therefore sum to zero. However, the sum of the longitudinal momenta can vary appreciably, as can the net longitudinal velocity of the collision event. According to the theory of special relativity, differences in θ between events will appear different to different observers depending on their relative longitudinal velocity. In other words, differences in θ are not Lorentz invariant.

Differences in a related quantity called the *rapidity*, defined as

$$\text{rapidity} = \frac{1}{2} \ln \frac{E + p_L}{E - p_L}, \quad (2.3)$$

are Lorentz invariant. Particle production in LHC collisions is roughly constant as a function of rapidity, and because differences in rapidity do not depend on the longitudinal speed at which one is moving, that statement is independent of whether the collisions are observed in their own rest frame or in that of the CMS. At very high energies, rapidity becomes approximately equal to the *pseudorapidity* η defined

by

$$\eta = -\ln \tan (\theta/2). \quad (2.4)$$

Since θ only depends on the position of the detector component in which a particle is measured, η serves as a convenient coordinate to describe the kinematics of high-energy pp collisions in a Lorentz-invariant way. Pseudorapidity begins at 0 for particles emitted from the IP exactly perpendicular to the beam, and rises in magnitude for particle trajectories more closely aligned with the beam axis, diverging to infinity as θ approaches 0.

The CMS has approximately hermetic coverage of particles emerging from the IP with $|\eta|$ up to 5.0, giving a total polar coverage of 178.46 degrees along with complete 360-degree azimuthal coverage. Particles emerging within this zone of coverage are detected with high probability by at least one subsystem, although the measurement quality varies as a function of $|\eta|$. Since particles are emitted with a roughly constant concentration as a function of η , and because cones of constant η become more densely packed at higher values of $|\eta|$, it follows that the intensity of particle radiation impinging on detector elements is stronger at higher $|\eta|$. Tradeoffs must be made between the measurement quality of an apparatus and its radiation hardness, and therefore equipment installed at higher $|\eta|$ is typically less precise.

2.2.2 Superconducting solenoid and silicon tracking system

The “S” in CMS derives from the 12.5-m-long, 0.3-m-thick, 6-m-inner diameter solenoid surrounding the core of the experiment. When an 18 kA current is applied to its more than 2000 windings of superconducting cable, it produces a homogeneous 3.8 T magnetic field in its center. The field is returned in the opposite direction with about half the magnitude by an iron return yoke surrounding the solenoid, consisting

of three barrel layers split into five wheels, complemented by three endcap disk layers at each end.

The size and shape of the solenoid are a primary design constraint for CMS. The HCAL, ECAL, and inner tracker together must be compact enough to fit completely inside it, giving rise to the “C” in CMS. Because of the cylindrical shape of the solenoid, all primary detector layers in CMS are divided into cylindrical barrel sections complemented by flat circular endcaps on either end.

The magnetic field produced by the solenoid is illustrated in Fig. 2.6. Charged particles traveling through this field have their trajectories bent, and at 3.8 T the field will noticeably bend even very high-momentum particles. This allows the ratio of a particle’s momentum to its charge to be measured, as particles with higher momentum are bent less than particles with the same charge but lower momentum. It also allows the sign of a particle’s electrical charge to be identified, as positively- and negatively-charged particles are bent in opposite directions (and electrically neutral particles are not bent at all).

The trajectories of charged particles close to the IP are mapped by an inner silicon tracking system, the innermost detector layer of CMS. It is based on tracking elements made from radiation-hard silicon, allowing high-speed measurements. Charged particles passing through the silicon tracker elements release bursts of free electric charge in the silicon. An applied voltage causes the charge to migrate to a detector at the edge of the element, allowing it to infer the time and location of the hit. Fine-grained position and time resolution is obtained by subdividing the tracker volume into tens of millions of separate tracking detector elements spread over multiple layers. Figure 2.7 illustrates the arrangement of tracker layers.

The inner tracker is subdivided into a pixel tracker surrounded by a strip tracker. The pixel tracker is the first CMS module that low- $|\eta|$ ($\lesssim 2.5$) particles pass through.

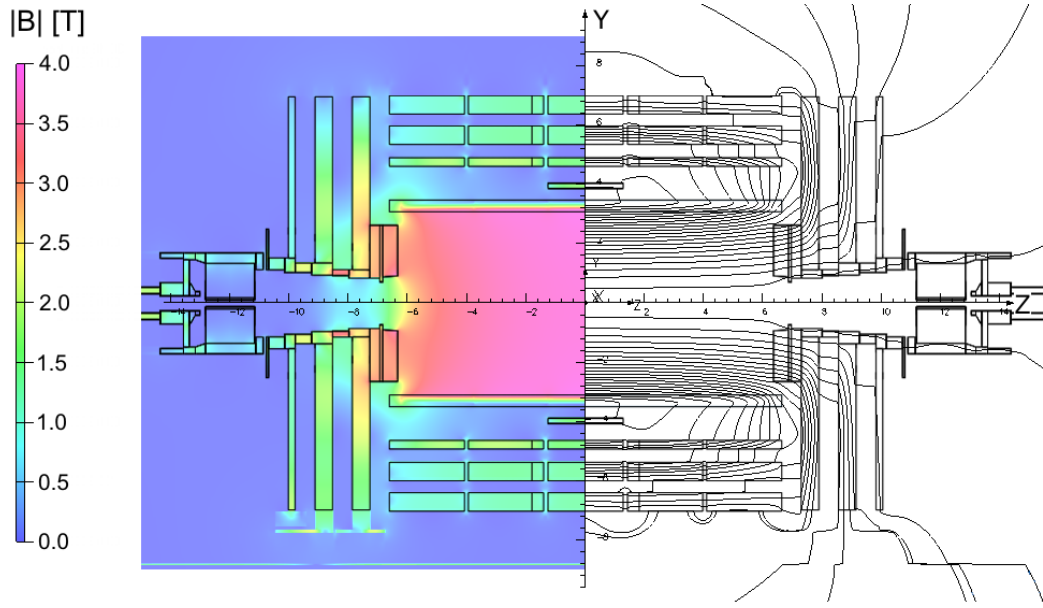


Figure 2.6: Magnetic field produced by the CMS solenoid, from [84]. The field strength in T is shown on the left, and contour lines smoothly connecting the field direction are shown on the right.

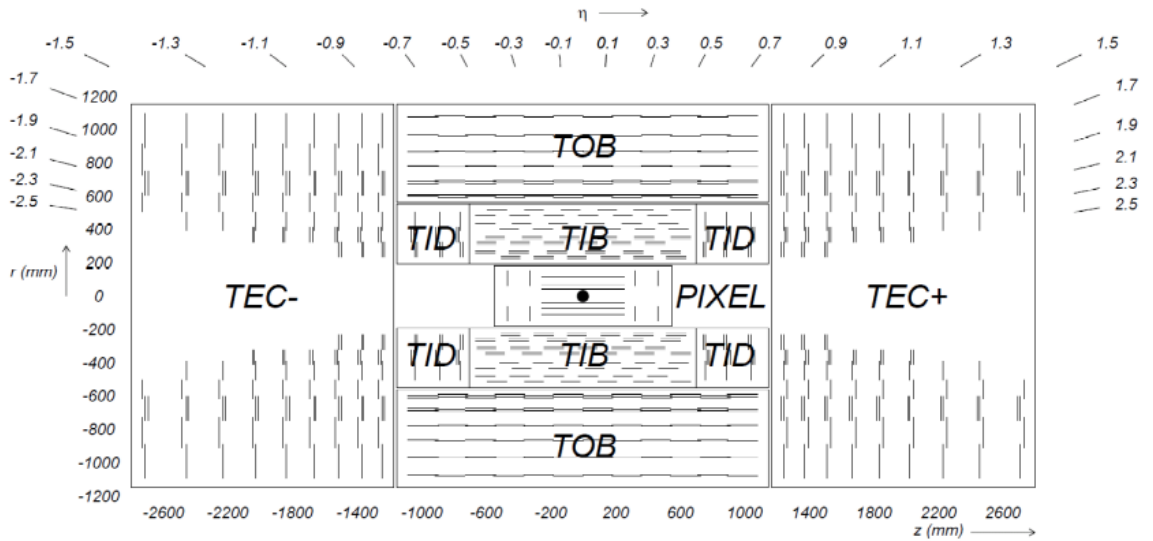


Figure 2.7: Arrangement of layers in the inner tracker.

It is subdivided into three barrel layers at $r = 4.4$, 7.3 , and 10.2 cm, and two endcap disks on each side at $|z| = 34.5$ and 46.5 cm. These layers are arranged so that at least three are hit by any particle with $|\eta| < 2.5$. The tracking elements comprise 66 million pixels, 48 million in the barrel layers and 18 million in the endcap disks, each with an area of $100 \times 150 \mu\text{m}^2$.

The strip tracker is subdivided into an inner barrel (TIB), inner disks (TID), outer barrel (TOB), and endcaps (TEC). The TIB consists of four cylindrical layers, capped by the TID which comprises three circular disks on each side of TIB. Together, TIB and TID extend from $r = 20$ cm to 50 cm and out to $|z| = 90$ cm. The TOB surrounds the TIB and TID and consists of six cylindrical layers. The TEC caps both TOB and TID and comprises nine circular disks on each side, complementing the TOB's radial coverage out to $r = 114$ cm and extending the $|z|$ coverage to 280 cm. The inner radius of TEC tapers upward with increasing radius so as to approximately adhere to the line $|\eta| = 2.5$. All together, the tracking elements comprise 9.3 million silicon strips, each with an area of $80 \times 180 \mu\text{m}^2$.

Both the pixel and strip trackers have hermetic coverage up to $|\eta| = 2.5$. Charged particles with $|\eta|$ in this range will tend to leave deposits in multiple layers of the inner tracker. By linking these sequential deposits together, the particle's trajectory through the inner tracker may be inferred.

2.2.3 Electromagnetic calorimeter

The electromagnetic calorimeter (ECAL) is the second main detector layer, after the inner tracker. It comprises 75 848 lead tungstate (PbWO_4) crystals, divided among a cylindrical barrel section (EB) and two endcap sections (EE). The overall structural organization of the ECAL is shown in Fig. 2.8.

The barrel extends to $|\eta| = 1.479$, and its 61 200 crystals are arranged in 170

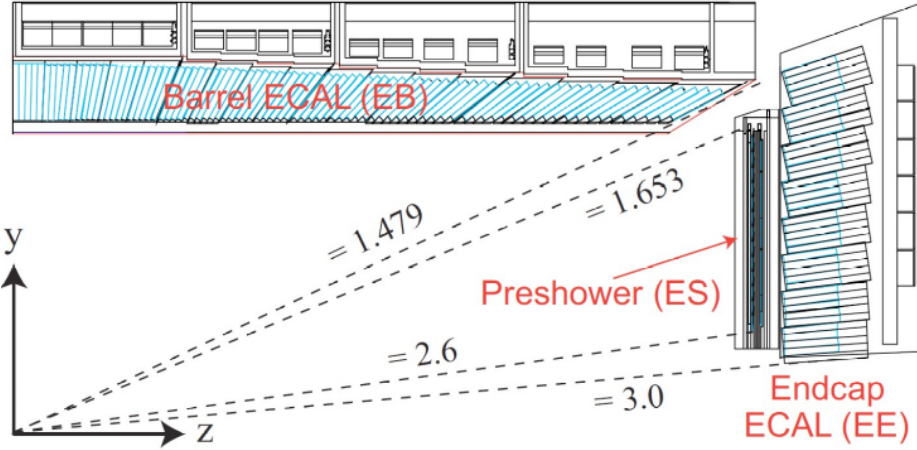


Figure 2.8: Schematic illustration of the ECAL, showing the longitudinal arrangement of crystals in the barrel and endcap sections.

wheels of 360 crystals each. Every ECAL crystal is shaped like a long, tapered rectangular prism with one larger, exterior square face attached to a sensor, and a smaller interior square face generally pointing toward the inner tracker. Crystals in EB are 23.0 cm long, with a $22 \times 22 \text{ mm}^2$ interior face and $26 \times 26 \text{ mm}^2$ exterior face. These proportions ensure a constant coverage of approximately 0.0174 in both η and ϕ along the entire length of the crystal. The center of each interior face sits at $r = 1.29 \text{ m}$. The crystals lie approximately along projective lines, i.e. lines directed toward the IP. To ensure fully hermetic coverage of particles leaving the IP, they are tightly packed with 0.35–0.50 mm of separation between adjacent crystals, and are tilted by 3 degrees off of the true projective line.

The remainder of the ECAL comprises two endcap disks of 7324 crystals each, covering $1.479 < |\eta| < 3.0$. Crystals in EE are each 22.0 cm long with a $28.6 \times 28.6 \text{ mm}^2$ interior face and $30 \times 30 \text{ mm}^2$ exterior face. The rectangular crystals are stacked in an approximation of a circle. They point along projective lines, directed not at the IP, but rather at a point on the beam axis 1.3 m past the IP. The interior edges of

EE sit at $|z| = 315.4$ cm when the experiment is running².

Lead tungstate crystal is a scintillator, producing visible light in the range of 430 nm (blue-green) in response to the passage of photons and electrons. The blue-green scintillation light travels freely through the optically transparent crystal, and sensors affixed to the outer face of each crystal collect this light. While its light output is not as high as some other scintillators (at maximum crystal transparency, about 4.5 electrons per incident MeV are collected by the sensors), PbWO_4 was the material of choice due to its high radiation tolerance, short radiation length ($X_0 = 0.89$ cm), and small Molière radius (2.2 cm).

High-energy electrons (or antielectrons) passing through a high atomic number material such as Pb or W will tend to lose energy in discrete bursts via the emission of photons (a phenomenon called *bremsstrahlung*, “braking radiation”), and high-energy photons will tend to propagate freely until suddenly decaying into an electron–antielectron (e^+e^-) pair. The *radiation length* X_0 is both the mean distance over which an electron has its energy reduced by bremsstrahlung by a factor of $1/e$, as well as $7/9$ of the mean free path for photons before they convert to an e^+e^- pair.

The products of a photon conversion are themselves high-energy electrons and antielectrons, and bremsstrahlung photons tend to have high energies as well, resulting in a stochastic sequence of photon emissions and e^+e^- pair production events called an *electromagnetic shower*. As the shower propagates through a given material, it spreads outward in a roughly conical shape with a characteristic average width. The *Molière radius* of a material is defined to be the radius of a cylinder, aligned with an electromagnetic shower, encompassing an average of 90% of the shower’s energy.

By conservation of energy, the total shower energy is the same as the energy of the original e or γ , and by conservation of momentum, the mean direction of the

²The intense magnetic field of the solenoid measurably constricts the CMS detector apparatus, pulling in EE by an estimated 1.6 cm.

shower is also the same as that of the original e/γ . The long depth of the crystals relative to their radiation length— $25.8 X_0$ in EB, $24.7 X_0$ in EE—ensures that nearly 100% of incident e/γ stemming from pp collisions leave electromagnetic showers that are fully contained by the ECAL, allowing their energies to be reliably inferred. The small Molière radius of PbWO_4 allows their orientation to be accurately judged, and nearby showers can be reliably separated in most cases.

The scintillation light is collected in EB crystals by avalanche photodiodes (APDs), and in EE crystals by more radiation-tolerant vacuum phototriodes (VPT). The amount of light collected is directly proportional to the shower energy contained in the crystal. The time of arrival of the shower is inferred by fitting a pulse shape to input signals collected every 25 ns. It takes time for the crystal scintillation to fully die down—after 25 ns, about 80% of the total scintillation light has been emitted—so the full pulse shape is spread over more than one input.

Free neutrons produced in the calorimeters can migrate through the detector and interact with a layer of epoxy used to affix the APD to the crystal surface, ejecting protons directly into the APD active volume. This triggers the release of thousands of electrons into the APD, resulting in a spurious signal that can be mistakenly reconstructed as an e/γ deposit with very high energy [85]. Since these *spikes* occur in single crystals, most can be distinguished from real e/γ showers by their narrow distribution of shower energy, as illustrated in Fig. 2.9. The APD does not receive a continuous light signal from the crystal scintillation in these events, so the pulse shape is constructed from only one input signal, as illustrated in Fig. 2.10. This has the net effect of shifting the inferred time of arrival backward, and most spikes have a measured arrival time between 10 and 15 ns before real photons in a given bunch crossing. “Double spikes” involving two neighboring crystals have also been observed, presumably arising from a secondary nucleon ejected by the primary neutron. These

are similarly distinguishable from real e/γ showers by their narrow energy distribution and early arrival time.

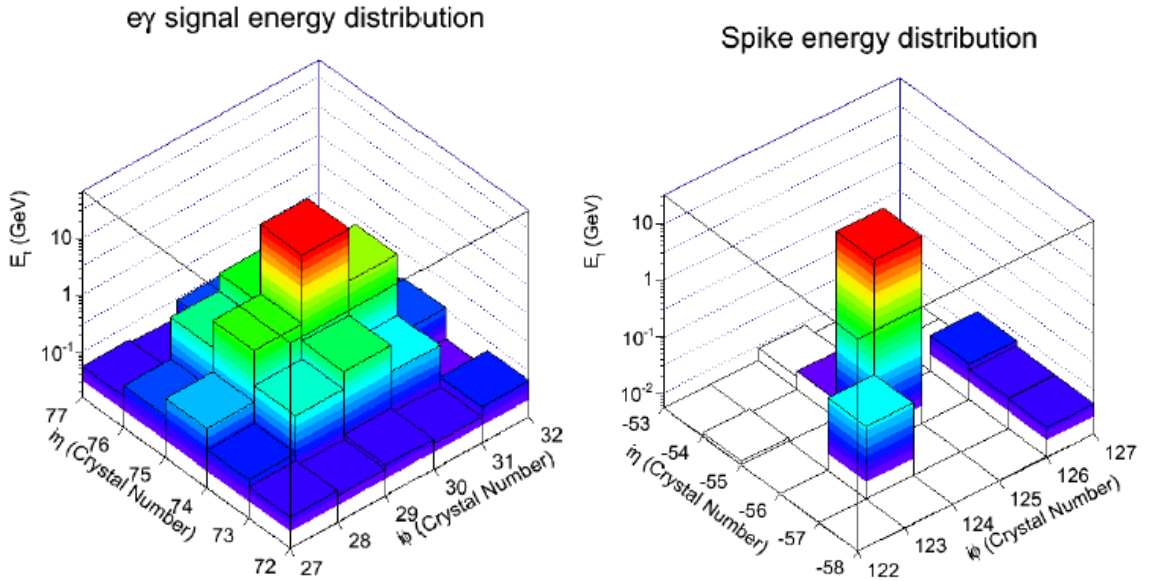


Figure 2.9: Distributions of electromagnetic shower energy among neighboring ECAL crystals. The distribution from an actual e/γ shower is shown on the left, and a spike distribution is shown on the right. From [86].

Neutral pions (a type of hadron produced copiously in pp collisions) decay rapidly into two photons, and when the pion is traveling at high speed, these photons will emerge moving in very close to the same direction. Despite the relatively small Molière radius of $PbWO_4$, it can still be difficult to discern whether the ECAL has been struck by a single high-energy photon or two tightly-collimated photons from a pion decay. To facilitate the identification of these pions, a preshower detector is installed on the EE.

The preshower comprises two modules, one attached to the inner edge of each ECAL endcap. A module consists of two layers, each with a lead radiator followed by a silicon strip sensor, and has a total thickness of 20 cm, covering $1.653 < |\eta| < 2.6$. The inner lead layer initiates electromagnetic showers from incoming e/γ particles,

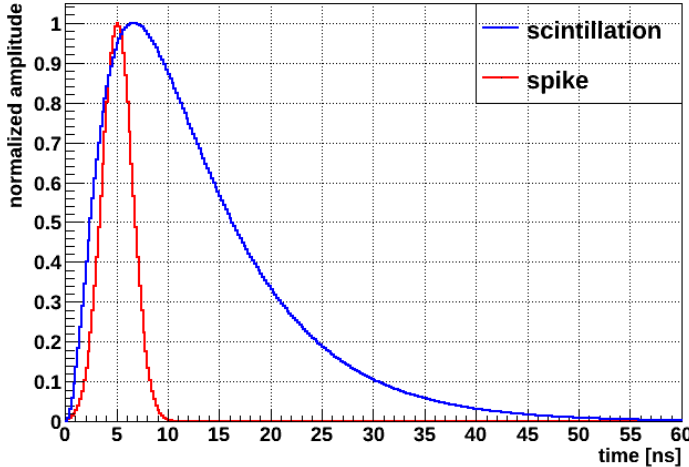


Figure 2.10: Pulse shapes in the APD produced by spikes and by genuine electromagnetic showers, from [87].

and the silicon sensor behind it measures the shower shape and energy. The second layer of lead continues the shower evolution, and the second layer of sensors provides another measurement. This is an example of a sampling calorimeter, and the same general strategy is employed by HCAL, described in the following section.

2.2.4 Hadronic calorimeter

After the ECAL, the next layer a particle will encounter is the hadron calorimeter (HCAL)³. The HCAL is subdivided into three main systems: the barrel (HB), endcap (HE), and forward calorimeters (HF). Figure 2.11 shows their overall layout.

The barrel and endcap systems are sampling calorimeters with alternating layers of brass absorber and plastic scintillator. The brass in the absorbers is an alloy of 70% Cu and 30% Zn. High-energy hadrons hitting the nuclei in these atoms can eject a number of secondary hadrons, which themselves can eject further hadrons in a cascade known as a *hadronic shower*. Like electromagnetic showers, hadronic showers

³If the particle has $|\eta| > 3.0$, the forward portion of HCAL is the first and only CMS detector layer it hits.

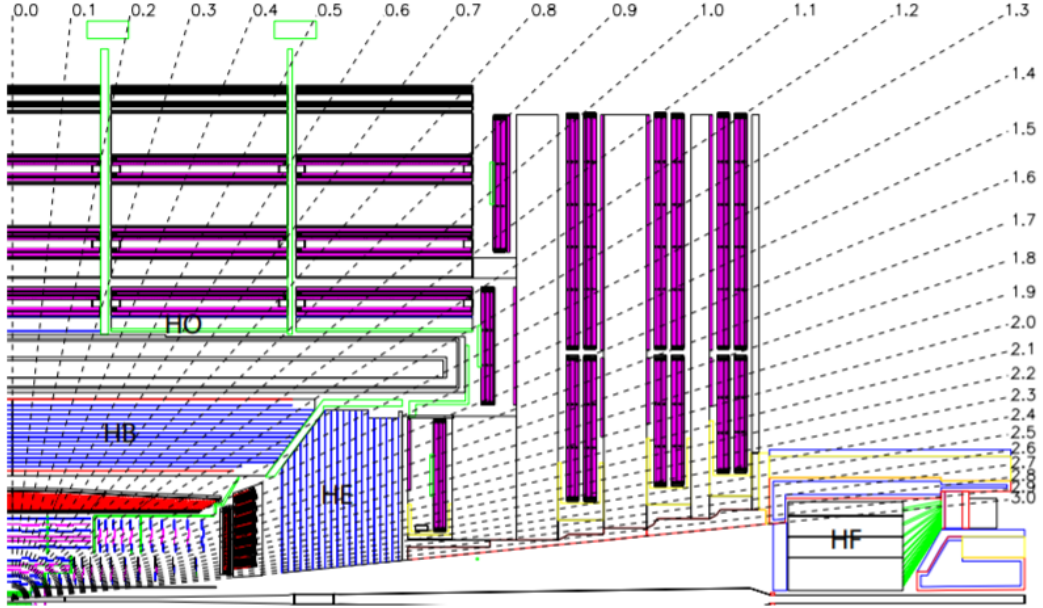


Figure 2.11: Schematic illustration of the HCAL overlaid with dashed lines of constant η , from [75]. Indicative arrangements of the muon systems, solenoid, ECAL, and inner tracker are also shown.

have a characteristic length, the *nuclear interaction length* λ_I . Hadrons such as pions can also decay midflight into high-energy e/γ , leading to secondary electromagnetic showers. The brass absorbers have $\lambda_I = 16.42$ cm and $X_0 = 1.49$ cm.

Absorber layers are interleaved with plastic scintillator tiles, with about 70 000 in total distributed between HB and HE. Inlaid fiber optic cables sample the scintillation light and carry it to hybrid photodiode (HPD) sensors. Up to 17 layers of plastic scintillator are stacked against each other in HB and HE, interleaved by brass absorber layers.

The barrel section covers $|\eta| < 1.3$. Layers of HCAL scintillators and absorbers lie parallel to the beam line. Towers of related scintillator tiles are grouped along projective lines pointing toward the IP, as shown in Fig. 2.12. In HB there are 16 tower divisions in η on either side of $\eta = 0$, and 72 tower divisions in ϕ , such that each tower has an $\eta\text{--}\phi$ coverage of 0.087×0.087 . The brass and scintillator layers are

separated into wedges in ϕ . So as to ensure hermetic coverage throughout HB, the brass layers within each wedge are staggered, and adjacent wedges are separated by less than 2 mm.

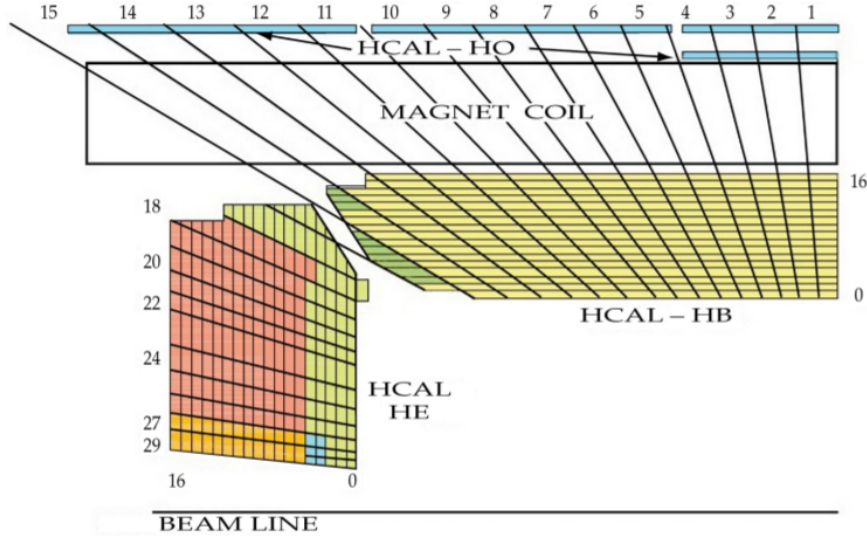


Figure 2.12: Arrangement of HB, HE, and HO towers, from [75].

The effective thickness of HB ranges from $5.39 \lambda_I$ at tower 0 to $10.3 \lambda_I$ at tower 15; tower 16 partially overlaps with HE. About 1.1 additional λ_I are supplied by the ECAL. The thickness of HB is constrained by the available space between EB and the solenoid. In order to provide a more robust measurement of shower energy, and also to supply additional insulation to the outer muon systems by capturing hadrons exiting the rear of HB, HCAL is supplemented by an outer barrel layer (HO) directly behind the solenoid. The solenoid itself contributes about $1.4 \lambda_I$ at low $|\eta|$.

The endcaps cover $1.3 < |\eta| < 3.0$. Like HB, the layers in HE are staggered so as to provide hermetic coverage. Unlike HB, no additional outer layer is needed, since HE is about $10 \lambda_I$ thick over its entire span. Towers in EE have a coverage of 0.087×0.087 for $|\eta| < 1.6$ and approximately 0.17×0.17 for $1.6 < |\eta| < 3$.

The HF covers the forward region, $3 < |\eta| < 5$. It is composed mostly of steel

with embedded quartz fiber, built in a cylindrical shape with a radius of 130.0 cm. The cylinder’s inner face sits 11.2 m from the IP and it extends 165 cm longitudinally, supplying approximately $10 \lambda_I$ for the development of hadronic showers. The intense radiation in the forward region necessitated the use of quartz fibers as the active medium for shower energy probing. High-energy charged particles in these showers generate Cherenkov light as they pass through the fibers, which run from front to back through the cylinder, and serve as fiber optic cables carrying that light to photomultiplier tubes. Half of the fibers run over the full length of the steel cylinder, and the other half begin 22 cm back from the inner face, allowing e/γ (which deposit most of their energy in the first 22 cm) to be distinguished from hadrons (which deposit their energy roughly equally before and after 22 cm). The fibers are bundled in towers, each with an $\eta\text{-}\phi$ coverage of 0.175×0.175 . For additional radiation protection, the HF is enclosed by layers of steel, concrete, and polyethylene shielding, up to 85 cm thick on the sides.

2.2.5 Muon systems

The “M” in CMS reflects the central role of muon detection and measurement in the design of the experiment. High-energy muons are minimum-ionizing particles (MIPs), reaching the outer muon systems largely unaffected by their passage through the inner detector layers. In contrast, most other particles are fully absorbed by more than $16 \lambda_I$ of material in the inner layers, leaving a relatively background-free environment in the muon chambers.

The muon chambers interleave the steel flux-return yoke, which in addition to concentrating the exterior magnetic field also serves to block other remnant particles from reaching the chambers. The layout of muon chambers is shown in Fig. 2.13. Like other CMS layers, the muon system is divided into a central barrel section and

two endcaps. The barrel section is instrumented by four layers of drift tube (DT) chambers, which cover $|\eta| < 1.2$. Each layer contains 8 chambers that measure the muon coordinates in the $r\text{-}\phi$ plane, and the inner three layers have an additional 4 chambers to measure the muon coordinate in the z axis.

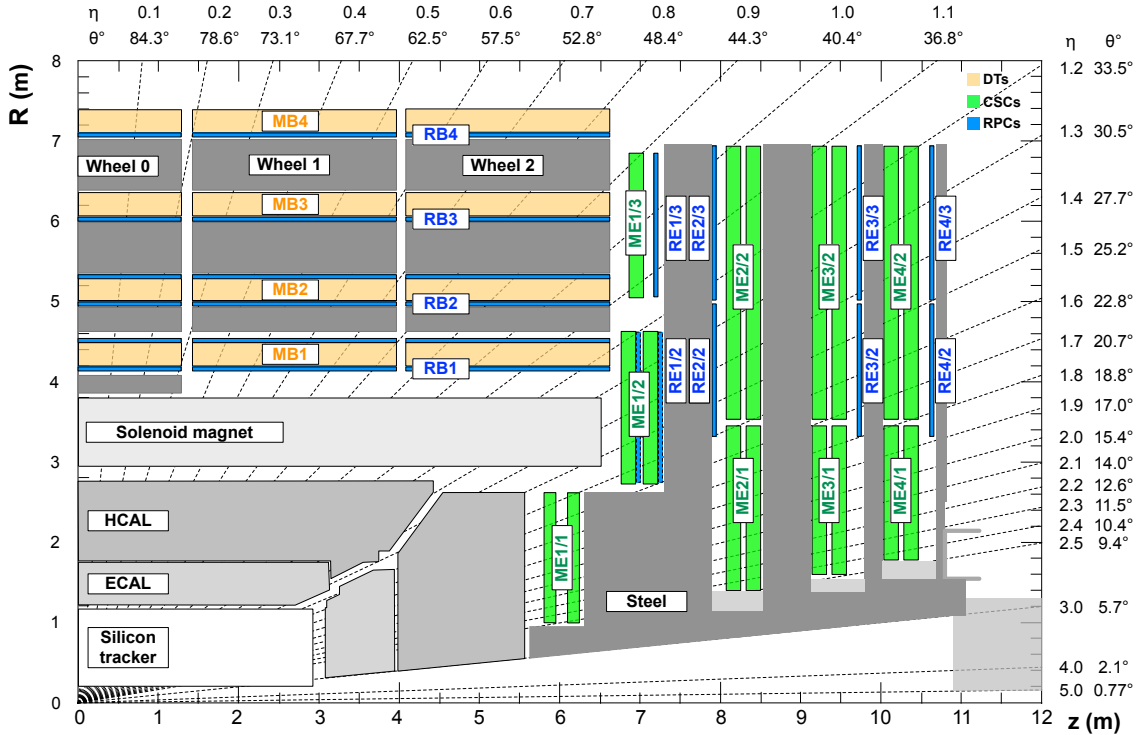


Figure 2.13: Muon systems in a quadrant of CMS. Indicative arrangements of the solenoid, HCAL, ECAL, and inner tracker are also shown.

The endcaps, subject to higher radiation fluences and more nonuniform magnetic fields, are instrumented by four layers of cathode strip chambers (CSCs), which cover $0.9 < |\eta| < 2.4$. Cathode strips, oriented in the radial direction, give a measurement in the $r\text{-}\phi$ plane, and anode wires running perpendicular to the strips provide an additional measurement of the muon η .

During the design of CMS, the reliability of time measurements from these two systems of muon chambers was highly uncertain, and thus a third system consisting

of resistive plate chambers (RPCs) was installed. These provide a relatively coarse position measurement, but a highly accurate time measurement. Muons with $|\eta|$ up to about 1.7 will pass through at least 4 RPC layers.

2.2.6 Trigger system

Data readout from the detectors occurs at a rate of 40 MHz (once every 25 ns), corresponding with the LHC bunch crossing frequency. The memory needed to store the full data produced in one collision event is about 1 MB, and it is presently impossible to extract or store data collected at a rate of 40 million MB/s. Therefore, the data is first filtered through a *trigger* system, which rapidly decides which events to store and which to discard.

The trigger system proceeds in sequential levels. The Level 1 (L1) trigger uses a reduced set of detector information to make an initial, extremely rapid (within 4 μ s) filtering decision at the rate of 100 kHz. Meanwhile the full detector data sits in a buffer. If the L1 accept (L1A) is given, that data is sent to the High-Level Trigger (HLT); otherwise it is discarded. The HLT uses the full data to make a less time-intensive, more sophisticated decision. Events accepted by the HLT have their data permanently stored.

The L1 trigger consists of custom hardware connected by fiber links to the CMS muon and calorimeter systems⁴. Information from HCAL and ECAL is sent through a dedicated calorimeter trigger pipeline, and information from the muon systems is sent through a separate muon trigger pipeline. The output of both of these pipelines is evaluated by a Global Trigger (GT), which makes the final L1A decision. The organization of L1 pipelines is illustrated in Fig. 2.14.

⁴Information from the inner tracker is not presently used by L1.

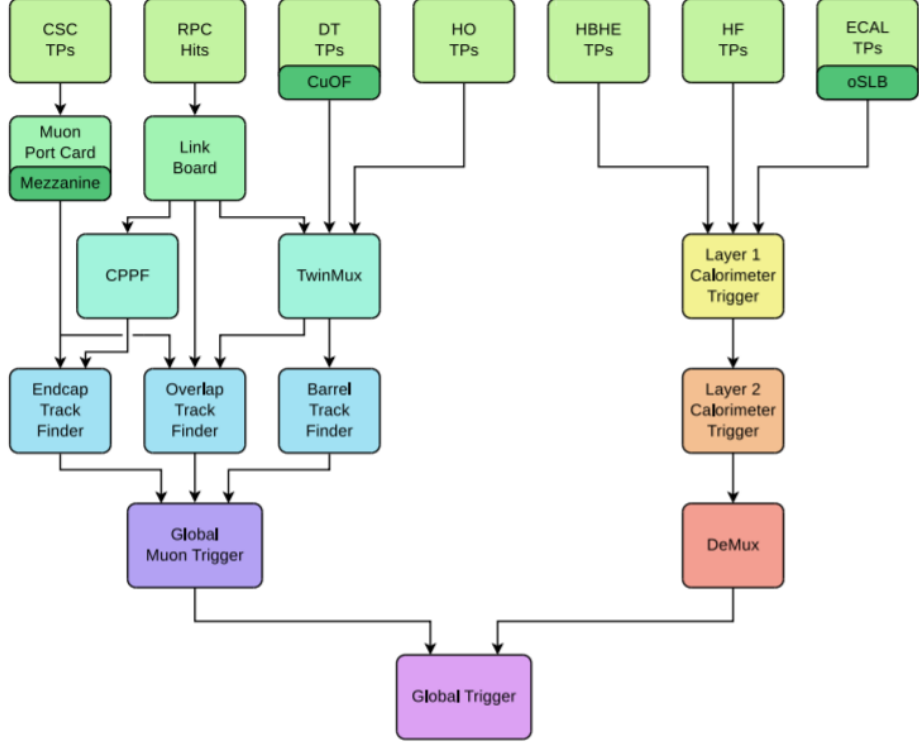


Figure 2.14: Schematic diagram of the L1 trigger pipeline.

The *trigger primitives* (TPs) sent by HCAL and ECAL are transverse energy sums recorded in calorimeter towers. These along with some quality information are sent to Layer 1 of the calorimeter trigger, which performs preprocessing, energy calibration, and the computation of some simple values. Layer 2 uses this information to construct various physics objects—L1 Jets, Taus, and EGamma⁵—using simple and fast reconstruction algorithms. Layer 2 comprises 9 parallel cards which analyze sequential events in a round-robin, “time-multiplexed” fashion, so as to give each card adequate memory and processing time for each event. The demultiplexer (DeMux) organizes the resulting output and sorts the L1 objects by p_T , sending this information along to the GT.

⁵With only calorimeter information, it is difficult to distinguish e from γ . In full offline event reconstruction, this classification is refined by incorporating inner tracker information.

The TPs from CSCs and DTs are track segments. Along with hits recorded in the RPCs, muon system TPs are routed through a lattice of preprocessor layers and then sent to dedicated Barrel, Endcap, and Overlap Track Finders covering different η regions. These rapidly assemble L1 Muon objects and send them to the Global Muon Trigger, which sorts the L1 Muons by p_T and quality, finally sending this information along to the GT.

The GT tests the L1 objects it receives against a set of L1 trigger paths, which specify various event selection criteria. After evaluating which trigger paths have been passed, the GT makes the final L1A decision. The time from TP generation to L1A decision cannot be longer than 4 μ s, and the overall L1A rate cannot be higher than 100 kHz; in 2016, this was the typical L1A rate actually achieved.

If the L1A is given, the full detector data is sent to the HLT, which consists of software running on commercial computing hardware. The HLT tests each event against a set of high-level trigger paths. Each of these paths has access to raw detector information as well as quantities computed at L1. Enough time and memory are available to perform a reduced sequence of the full offline event reconstruction algorithms, separately optimized for each path. In 2016, the average HLT processing time per event was less than 160 ms, and the typical HLT accept rate was 1 kHz.

2.2.7 Luminosity measurement

In principle, the integrated luminosity is given by integrating the instantaneous luminosity defined by Eq. 2.2 over the data taking period, with an extra efficiency factor to account for the fraction of time during which the trigger was active. In practice, the uncertainty on the parameters of Eq. 2.2 is fairly high, and more precise measurements of instantaneous luminosity are obtained by directly examining the beam intensities.

In the method developed by van der Meer [88], the two beams are scanned across each other in the transverse plane, giving a direct experimental probe of the beam profile that is used to calibrate the relationship between instantaneous luminosity and specific observables accessible to various beam monitoring instruments. A van der Meer scan establishes the calibrated visible cross section σ_{vis} of a process examined by each luminometer, such that the instantaneous luminosity measured by a luminometer is given by

$$\mathcal{L} = R/\sigma_{\text{vis}} \quad (2.5)$$

where R is the observed rate of the process measured by the luminometer. The pixel tracker, DTs, and HF are used for this purpose, in addition to two dedicated instruments: the Fast Beam Conditions Monitor (BCM1f) and Pixel Luminosity Telescope (PLT).

Van der Meer scans require dedicated LHC runs outside of normal data taking, but the calibrated luminometers continue to monitor the beam luminosity during physics runs. The uncertainty on calibrated luminosity measurements in 2016 data taking is 2.5% [89]. The data set used in this thesis corresponds to a time-integrated luminosity $L = 35.9 \text{ fb}^{-1}$.

Chapter 3

Simulation

3.1 Parton distribution functions

A hard collision involving a proton can cause individual partons within it to be clearly resolved. For collisions with characteristic energy Q , the probability that the parton will be of type i and carry a fraction x of the proton's total momentum is given by a function $f_i(x, Q^2)$ known as a parton distribution function (PDF).

The dependence of these functions on Q is described by the DGLAP equations [90–92], which are derived from the theory of QCD. These allow the specific values of $f_i(x, Q^2)$ to be calculated at arbitrary Q as long as they are first measured at some particular Q . Like cross sections, the DGLAP equations, and hence PDFs derived in this way, admit perturbative expansions out to specific orders in α_S [93].

Simulated samples used in this thesis use PDFs computed to different orders as appropriate for the order of the cross section used. Samples with cross sections computed to LO in α_S use the NNPDF3.0 LO PDF set [94]. Samples with NLO cross sections, as well as theoretical $Z(\nu\bar{\nu})\gamma$, $W(\ell\nu)\gamma$, and $Z(\ell\ell)\gamma$ cross sections computed to NNLO in MATRIX, use the NNPDF3.1 NNLO PDF set [95]. These PDF sets are based on

fits of the theoretical DGLAP functional form to the experimentally-measured values of the PDFs from multiple experiments, examining a variety of processes at a range of different energy scales.

3.2 Hard process generation

A generic hard proton scattering process proceeds as

$$p + p \rightarrow X + \text{rest} \quad (3.1)$$

where X is a high-energy final product (such as a γ) of a hard parton–parton collision, and rest is a collection of lower-energy final-state hadrons emerging from softer parton interactions.

According to the QCD factorization theorem, the dominant contribution to the cross section σ_X of such a process is given by (see e.g. [2])

$$\sigma_X = \sum_{i,j} \int dx_1 dx_2 f_i(x_1, \mu_F^2) f_j(x_2, \mu_F^2) \sigma_{i,j \rightarrow X} \quad (3.2)$$

where i, j specify the types of the hard scattering partons, and $\sigma_{i,j \rightarrow X}$ is the cross section for the partonic process

$$i + j \rightarrow X + \text{rest} \quad (3.3)$$

which can be computed to a desired order using Feynman diagrams¹. The energy scale μ_F is called the factorization scale. The value of α_S , which appears in perturbative expansions of $\sigma_{i,j \rightarrow X}$, is governed by another energy scale μ_R called the renormalization scale². The coefficients of α_S in such perturbative expansions also

¹Here rest is a collection of quarks and gluons that eventually fragment into final-state hadrons.

²As the characteristic energy scale increases, the effective value of α_S decreases. This is in contrast to the fine structure “constant” α , whose value increases with increasing energy.

depend on μ_F and μ_R , in such a way as to completely cancel any μ_F, μ_R dependence in the exact formula for the total cross section σ_X [93].

The values of μ_F and μ_R do, however, affect the approximate cross section derived at a finite order in α_S . Typically these scales are chosen to be on the order of the parton–parton collision energy. The simulated samples used in this thesis were made by fixing both μ_F and μ_R to the mass of the Z -boson, about 91.2 GeV. This choice is a source of theoretical uncertainty, whose magnitude is estimated in this thesis by examining the variation of the final results when μ_F and μ_R are separately shifted up and down³ by a factor of 2.

Differentiating σ_X with respect to a kinematic variable such as p_T^γ yields $d\sigma_X/dp_T^\gamma$, the differential cross section for the process $p + p \rightarrow X + \text{rest}$ to occur with some specific final-state p_T^γ . For an elementary process like $i + j \rightarrow X + \text{rest}$, this may be analytically solved or numerically approximated out to a given order.

However, the full dynamics of a pp interaction and subsequent interactions of the products with the CMS detector do not admit simple solutions. These and other integrals over probability distributions may be estimated via the Monte Carlo (MC) method. Many random events⁴ are generated according to known probability distributions, and the integrand (e.g. some reconstructed kinematic quantity) is evaluated for each event. The sum of the integrand values for each event within a given kinematic region, divided by the total number of events generated, gives an estimate of the integral within that region (e.g. the content of a bin in a histogram).

Matrix element (ME) generators allow for MC estimates of $d\sigma_X/dp_T^\gamma$ by generating partons with species and initial-state kinematics sampled according to the PDFs, and with final-state kinematics sampled according to the differential partonic cross

³Following common practice, correlated shifts up and down are also considered, but “unphysical” anticorrelated shifts (e.g. $2*\mu_F, 0.5*\mu_R$) are not [96].

⁴“Monte Carlo” alludes to an eponymous casino in Monaco.

sections $d\sigma_{i,j \rightarrow X}/dp_T^\gamma$. The ME generator for all simulated samples used in this thesis is MadGraph5_aMC@NLO [97], which also constructs the matrix elements for the elementary partonic processes. All⁵ samples are generated to LO in α_S . Since $Z(\nu\bar{\nu})\gamma$, $W(\ell\nu)\gamma$, and $Z(\ell\ell)\gamma$ are all generated to LO, their simulation does not incorporate Feynman diagrams with extra radiated quarks and gluons. These extra particles are known to appear at higher orders, and since they can substantially affect the kinematic balance and reconstruction efficiency of events, up to 2 of these are added by the generator to simulate their impact.

If it is decided that the probability of an event's occurrence should be changed by some multiplicative factor w , this can be simulated by multiplying a generated event's weight by w in any final sums. By this principle, uncertainties associated with the PDFs are represented in the NNPDF sets by 100 different weights on each event [94, 95]. The PDF uncertainty of a histogram estimated via MC is obtained by taking the sample standard deviation of each bin in the histogram with respect to these 100 weight variations [98].

The NNLO cross sections for $Z(\nu\bar{\nu})\gamma$, $W(\ell\nu)\gamma$, and $Z(\ell\ell)\gamma$ are estimated using the MATRIX generator [14], which incorporates NNLO ME results for $Z\gamma$ and $W\gamma$ processes derived in [9, 10, 99]. An LO-to-NNLO event weight is then applied to each event simulated in MadGraph, by taking the NNLO-over-LO ratio of the differential cross section $d\sigma/dp_T^\gamma$ integrated within a p_T^γ bin corresponding to the generated γ . An additional p_T^γ -dependent weight that accounts for NLO EWK corrections, computed in [7, 8], is also applied. The impact of these corrections is illustrated in Fig. 3.1.

To avoid numerical divergences that can arise in perturbative calculations, and also to avoid wasting computational cycles simulating events outside the analysis scope of this thesis, kinematic cuts are applied on the events that may be generated.

⁵Aside from a small subset of DM simplified model samples generated to NLO.

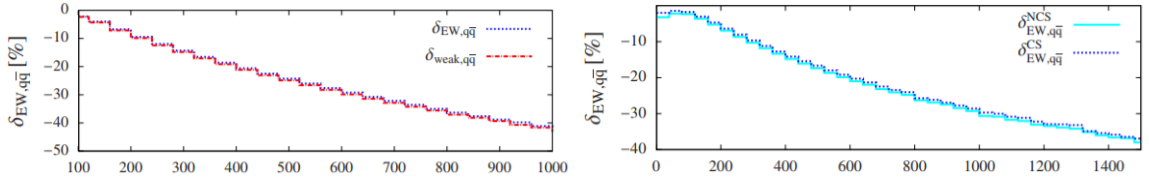


Figure 3.1: Fractional shifts on event weights introduced by NLO EWK corrections, as a function of p_T^γ . Left: $Z(\nu\bar{\nu})\gamma$. Right: $W(\ell\nu)\gamma$. From [7, 8].

Most significantly, BSM and $W, Z + \gamma$ events are only simulated if they have a leading γ with $p_T > 130$ GeV emitted within the ECAL acceptance. For consistency, the same generator-level cuts (as well as PDF sets) are applied in both MATRIX and MadGraph.

3.3 Parton showering and hadronization

The output of the hard collision, $X + rest$, continues to evolve as it exits the interaction point. For example, high-energy quarks and gluons will tend to radiate other high-energy quarks and gluons in a cascading process known as a parton shower, dispersing their energy as they do so. The energies of the showering partons begin at the hard interaction energy scale and go down to the hadronization scale ($\lesssim 10$ GeV). Above this energy scale, α_S is less than $O(1)$, and so the parton shower process admits a perturbative analysis in the theory of QCD. The statistical behavior of parton showering is governed by Sudakov form factors derived from the DGLAP equations [93].

Below the hadronization scale, the remnant partons will no longer have enough energy to freely split and will finally bind into hadrons in a process called hadronization. This occurs as the value of α_S associated with a typical parton energy rises above $O(1)$, rendering estimates based on perturbative expansions invalid. The bulk

of the partons in the colliding protons are not directly involved in the hard parton–parton scatter and are also subject to a nonperturbative energy scale; these contribute softer showers of particles⁶ known as the underlying event. These nonperturbative processes are simulated with generator-dependent phenomenological models, tuned to match the hadronic distributions observed in the experiment. For all the simulated samples used in this thesis, both parton showering and hadronization are handled by PYTHIA 8.218 [100], with underlying-event tune CUETP8M1 [101].

3.4 Pileup and detector simulation

The simulated contribution from pileup is estimated by overlaying additional “minimum-bias” events, with simulated particle distributions corresponding to the typical pp scattering events most likely to occur in the LHC. These are estimated by taking LHC collision data with no special trigger selections applied. This step of the simulation is also handled by PYTHIA.

The output of the preceding steps is a collection of several thousand stable or semistable particles that continue to propagate outward and interact with the detector. This stage is handled by GEANT4 [102], which simulates the decay of long-lived ($0.01 \text{ m}/c \lesssim \text{lifetime} \lesssim 10 \text{ m}/c$) particles within the detector volume, miscellaneous physical processes including those discussed in the previous chapter (magnetic bending, electromagnetic showers, hadronic showers, scintillation, etc.), and the response of detector electronics, leading to the final digitized detector output.

⁶The *rest* terms in the equations of sec. 3.2.

Chapter 4

Object reconstruction

4.1 The particle-flow algorithm

The goal of the particle-flow (PF) algorithm is to reconstruct the identities and kinematic properties of all final-state particles in an event. The CMS is the first hadron collider experiment to have successfully implemented this strategy, owing to its precise and robust tracking systems, highly granular and hermetic calorimeters, and intense solenoidal magnetic field. The PF algorithm is described in detail in [103].

Particles with lifetimes long enough to exit the beam pipe and reach CMS are divided into six general classes: electrons, photons, charged hadrons, neutral hadrons, muons, and neutrinos. Neutrinos do not interact with any of the detector layers, and so PF only attempts to directly reconstruct the other five classes. Electrons, charged hadrons, and muons leave tracks in the inner tracker, while photons and neutral hadrons do not. Photons and electrons deposit nearly all their energy in electromagnetic showers in ECAL, which completely stops them from propagating forward to subsequent detector layers. Generally speaking, hadrons and muons do not produce substantial ECAL showers, and these particles continue on to HCAL.

Hadronic showers usually begin in one of the calorimeters and evolve mainly in HCAL, which fully absorbs them before they can reach the muon detectors. Muons do not produce hadronic showers and, being MIPs, pass through the inner tracker, calorimeters, solenoid, steel flux-return yoke, and muon detectors largely unperturbed aside from magnetic bending, leaving tracks in the muon detectors on their way out. These interactions are illustrated in Fig. 4.1.

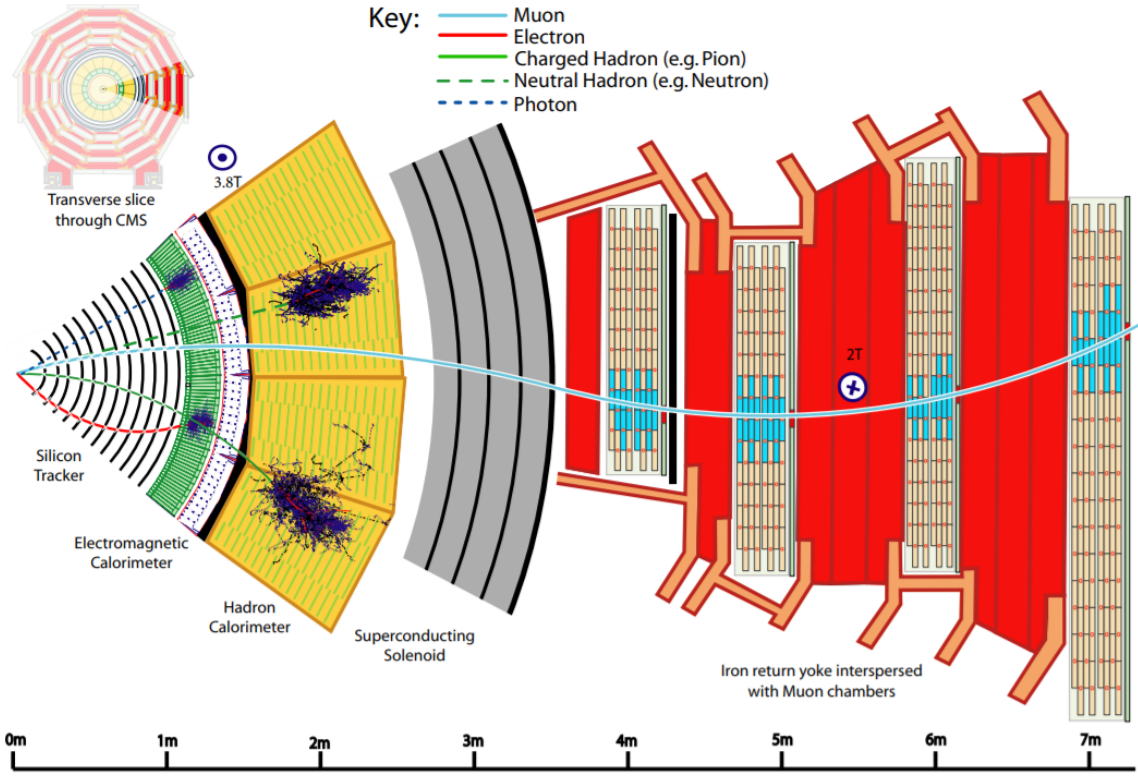


Figure 4.1: A schematic diagram of CMS overlaid with the classes of particles reconstructed by the PF algorithm, showing their most characteristic interactions with detector layers. From [103].

Each detector layer gives rise to basic characteristic elements used in event reconstruction: tracks from the inner and muon trackers, and clusters from the ECAL and HCAL. The PF algorithm links these elements together so as to deduce the species of a particle based on the set of elements present along its trajectory. The linked

elements corresponding to a given particle then provide multiple pieces of data on the particle’s behavior, which are synthesized in order to refine the measurement of the particle’s kinematic properties.

Like the physical detector and the trigger apparatus, the reconstruction algorithms employed by CMS are subject to ongoing evolution and optimization. The details given in this chapter correspond to the specific strategies used in 2016.

4.2 Tracks and clusters

Track reconstruction in the inner tracker is performed over 10 iterations, with the parameters of each iteration tuned to maintain a high selection purity and reconstruction speed. In each iteration, seeds comprising a few tracker hits are used to initiate an iterative trajectory building algorithm, which adds a tracker hit to the track according to the Kalman filter method, fits a trajectory to those hits, and then searches for additional hits compatible with the latest trajectory, until all tracker layers are exhausted [104]. Hits assigned to tracks in one iteration are then masked so as to reduce the probability of a misreconstructed track in successive iterations, allowing the track reconstruction efficiency to grow while simultaneously keeping the purity high. A separate muon track reconstruction algorithm is seeded by hits in the DTs and CSCs. Hits in the DTs, CSCs, and RPCs are linked along a potential muon trajectory, resulting in a standalone-muon track.

Clustering is performed separately in EB, EE, HB, HE, and each of the two preshower layers on either endcap¹. The algorithm proceeds in the same general fashion in each of these components, with distinct component-dependent threshold

¹Separate cells are not clustered in HF. Rather, each individual HF cell gives rise to one HF EM cluster and one HF HAD cluster, corresponding to the electromagnetic and hadronic components of each cell, respectively.

values [103] applied at various steps. Since this thesis focuses on barrel photons, only EB thresholds are reported here.

An EB crystal is identified as a cluster seed if its energy exceeds 230 MeV as well as that of its 8 immediate neighbors. Neighboring cells are progressively added to a topological cluster based on the seed, as long as their energy exceeds 80 MeV (twice the average noise level in EB) and they share at least one corner in common with a cell in the cluster. A single topological cluster can grow to encompass multiple seeds. Once a topological cluster is fully built, the energy distribution in the topological cluster is fit to a sum of Gaussian shapes, with one Gaussian of width $\sigma = 1.5$ cm per seed. Each of the fit shapes then becomes its own cluster, with a position and energy defined by the Gaussian's mean and amplitude, respectively. In this manner, the energy of a single crystal can be shared between distinct clusters.

A linking algorithm assigns a link between two PF elements if they lie near each other in the η - ϕ plane and satisfy some quality criteria. Linked elements are then chained together into lattices called blocks. A block corresponding to a simple isolated particle trajectory may have a simple linear topology, but generic blocks can have treelike structures with various converging and diverging lines. This reflects the tendency of particles to radiate or decay into other particles, as well as the possibility that multiple particles may be collimated so closely that their separate contributions to PF elements cannot reliably be distinguished by just the linking algorithm. Subsequent stages of the PF algorithm identify the particle(s) corresponding to each block using a sophisticated decision tree. The most robustly-reconstructed particles are identified first and have their contributions to PF elements subtracted out from those elements, leaving behind residual excesses which can then be identified as other particles.

4.3 Photons and electrons

Just prior to the installation of ECAL into CMS, the energy resolution of single electrons in the barrel region was estimated by firing an electron beam directly at the crystal array [105]. These measurements show that a 5×5 crystal array contains about 97% of an electron shower's energy. A fit of that data to the functional form²

$$\frac{\sigma}{E} = \frac{S}{\sqrt{E}} \oplus \frac{N}{E} \oplus C \quad (4.1)$$

gives $S = 0.028 \text{ GeV}^{1/2}$, $N = 0.12 \text{ GeV}$, and $C = 0.003$. This indicates that, using only ECAL shower information, a isolated e or unconverted γ with energy around 200 GeV can have its energy measured to within 0.4%.

This straightforward picture of a single e or γ hitting the ECAL is complicated by the significant depth of tracking material in front of it. As shown in Fig. 4.2, a minimum of $\approx 0.4 X_0$ of material sits in front of EB, rising up to $\approx 2 X_0$ near $|\eta| = 1.4$. On average, electrons will radiate away about 33% of their energy through bremsstrahlung near $|\eta| = 0$, and about 86% of their energy near $|\eta| = 1.4$ [106]. The electron trajectory is bent in the ϕ coordinate by the solenoid's magnetic field, but the radiated photon trajectories are not, so they are spread widely in ϕ . Meanwhile, photons have a substantial chance of converting to an e^+e^- pair in the tracker. These particles similarly have their trajectories bent in ϕ (in opposite directions) by the magnetic field, and they also radiate photons. The PF algorithm incorporates a dedicated conversion finder [107] to identify these cases.

Bremsstrahlung photons tend to emerge nearly parallel to the parent electron's motion, and so have momentum vectors lying tangent to the electron's track. As part of the linking algorithm, tangent lines from the track are drawn at each of its intersections with the tracker layers. If one of these tangent lines, extrapolated

²The symbol \oplus denotes addition in quadrature.

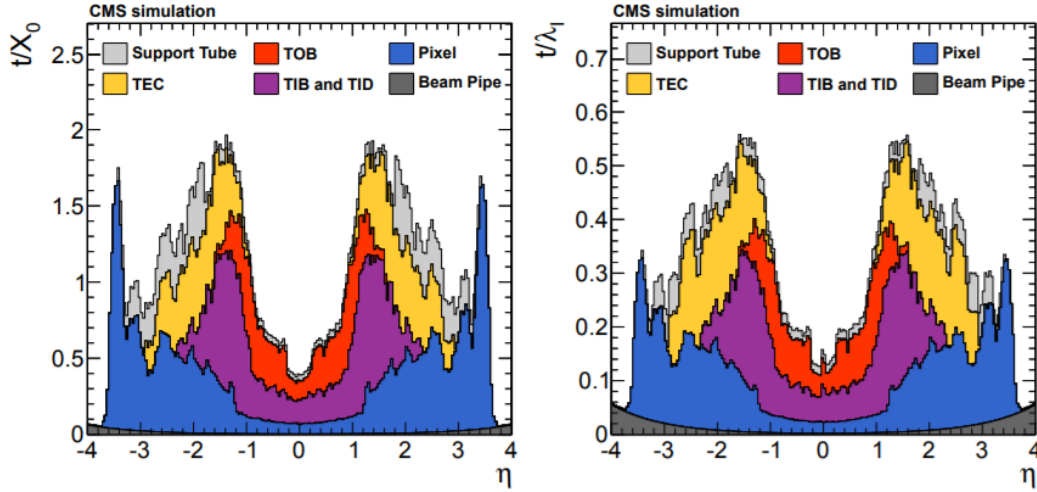


Figure 4.2: Thickness of material in front of ECAL, in multiples of X_0 (left) and λ_I (right). From [108].

forward, is compatible with the position of an ECAL cluster (or a conversion track pair identified by the conversion finder), the cluster (or track pair) is linked to the track as a possible bremsstrahlung photon.

Any energy recorded in the preshower detector is added to that of the closest ECAL cluster (or else discarded if no associated cluster is found).

A “Swiss cross” cut is applied in order to reject spikes: defining E_1 to be the energy of the seed crystal and E_4 to be the sum of the energies of the 4 neighboring crystals, a PF photon is only reconstructed if $E_4/E_1 > 0.05$. Double spikes are suppressed by a similar cut based on the ratio of E_2 , the sum of the energies of the seed crystal and its highest-energy neighbor, and E_6 , the sum of the energies of the six neighboring crystals surrounding the first two. Further spike rejection is achieved by requiring the time of energy deposits above 1 GeV to be within 2 ns of the bunch crossing time.

The response of calorimeter cells is periodically calibrated so as to faithfully reproduce the shower energy they contain. Due to the thresholds imposed in the clustering

stage, some of this energy will tend to be left out of PF clusters, and therefore another layer of calibrations is applied to these clusters in order to restore this energy. Bremsstrahlung and photon conversions introduce multiple additional particles to the event, with multiple opportunities for energy to be lost as particles escape through small cracks in the detector, fall into dead regions, etc. Thus, a third layer of particle-specific calibrations is derived for photons and electrons. The energy most commonly reported in CMS analyses is this final calibrated value.

Photons typically have their energies raised by up to a few percent by the last set of calibrations. However, after examining monophoton events with probable non-photon objects misreconstructed as photons, we have determined that these “fake” photons are often assigned very large energy shifts on the order of 100%, badly skewing their energies upward. This is due to the fact that fake photons tend to have atypical photon shower shapes, and the calibrations, based on simulated “real” photon events, were derived as a function of shower shape³. High- E_T^γ events have the least precisely measured cross sections, and are also the most sensitive probes of the BSM models examined in this thesis. In order to minimize contamination of this sensitive kinematic region, we have opted to use the uncalibrated “raw” photon supercluster E_T as the reconstructed quantity in which to bin our data.

4.4 Muons

A track in the inner tracker qualifies as a tracker-muon track if its extrapolated trajectory matches at least one hit in the muon systems. If an inner track fits together with a standalone-muon track, hits in both tracks are fit to a common global-muon track. About 99% of muons produced within the η coverage of the muon systems

³For this reason, calibrations derived in 2017 and 2018 are independent of shower shape [109].

are reconstructed as a global or tracker muon⁴. The additional hit data markedly improves the momentum resolution of muons with $p_T \gtrsim 200$ GeV [103].

A muon candidate is accepted as an isolated muon if the tracks and calorimeter deposits within $\Delta R < 0.3$ of the candidate muon have a total p_T no greater than 10% of the candidate muon p_T . A muon that fails this criterion can still be accepted as a nonisolated muon if it passes a “tight” muon ID, as defined in [103]. It can also be accepted if it has a high-quality global or inner track with a large number of hits, as long as any associated calorimeter clusters are compatible with the muon hypothesis.

Once a muon is accepted, its p_T is derived from its track. For high- p_T (> 200 GeV) candidates,

4.5 Jets and missing transverse momentum

As a consequence of parton showering and hadronization, a single radiated quark or gluon from a hard-scatter event does not reach the CMS detector as a single particle, but rather a collimated “jet” of hadrons (mostly pions) and their decay products (such as photons from neutral pion decays). The goal of a jet reconstruction algorithm is to identify which final-state particles arose in such a manner, group them according to their originating particle, and recover as accurately as possible the properties of the that particle.

The output of the PF algorithm is a set of basic particles of the five types described above. These serve as the input to the anti-kT algorithm

Discussion of jets is followed by a definition of p_T^{miss} and Type-1 p_T^{miss} corrections.

⁴They are often reconstructed as both. A separate global muon and tracker muon are merged into a single muon candidate if they share the same inner track.

Chapter 5

Event selection

5.1 The monophoton signature and background sources

Summarize how each of the physics processes being analyzed exhibits a monophoton signature. List the sources of background in the monophoton channel, to justify the ensuing cuts.

5.2 Trigger and p_T^{miss} filters

Trigger path, trigger efficiency

p_T^{miss} filters

5.3 Photon

Photon kinematic cuts; Photon ID defintion, efficiency; Spike and beam halo cuts; phoET-dependent cross section corrections

5.4 Missing transverse momentum

$p_T^{\text{miss}} > 170 \text{ GeV}$; $\Delta\phi(\gamma, \vec{p}_T^{\text{miss}}) > 0.5$; $\min\Delta\phi(\text{jets}, \vec{p}_T^{\text{miss}}) > 0.5$; $E_T^\gamma/p_T^{\text{miss}} < 1.4$

5.5 Lepton vetoes

Electron selection; Muon selection

5.6 Single electron control region

5.7 Single muon control region

5.8 Dielectron control region

5.9 Dimuon control region

Chapter 6

Background estimation

For each component, describe its estimation and uncertainties

6.1 Simulated backgrounds

6.2 Electron faking photon

6.3 Jet faking photon

6.4 Spikes

6.5 Beam halo

6.6 Transfer factors

6.7 Likelihood function

Chapter 7

Results

7.1 $Z(\nu\bar{\nu})\gamma$ cross section

7.2 aTGC limits

7.3 DM simplified model limits

7.4 ADD limits

Chapter 8

Conclusions

8.1 Summary

8.2 Outlook

Bibliography

- [1] F. Halzen and A. Martin, *Quarks & Leptons: An introductory course in modern particle physics*. John Wiley & Sons, 1984.
- [2] V. Barger and R. Phillips, *Collider Physics*. Westview Press, 1996.
- [3] M. Peskin and D. Schroeder, *An Introduction to Quantum Field Theory*. Westview Press, 1995.
- [4] M. Srednicki, *Quantum Field Theory*. Cambridge University Press, 2007.
- [5] M. Schwartz, *Quantum Field Theory and the Standard Model*. Cambridge University Press, 2013.
- [6] M. Tanabashi *et al.*, “The Review of Particle Physics,” *Phys. Rev. D* **98** (2018) 030001, doi:10.1103/PhysRevD.98.030001.
- [7] A. Denner, S. Dittmaier, M. Hecht, and C. Pasold, “NLO QCD and electroweak corrections to $W + \gamma$ production with leptonic W -boson decays,” *JHEP* **2015** (2015) arXiv:1412.7421, doi:10.1007/JHEP04(2015)018.
- [8] A. Denner, S. Dittmaier, M. Hecht, and C. Pasold, “NLO QCD and electroweak corrections to $Z + \gamma$ production with leptonic Z -boson decays,” *JHEP* **2016** (2016) arXiv:1510.08742, doi:10.1007/JHEP02(2016)187.
- [9] M. Grazzini, S. Kallweit, D. Rathlev, and A. Torre, “ $Z\gamma$ production at hadron colliders in NNLO QCD,” *Phys. Lett. B* **731** (2014) 204, arXiv:1309.7000, doi:10.1016/j.physletb.2014.02.037.
- [10] M. Grazzini, S. Kallweit, and D. Rathlev, “ $W\gamma$ and $Z\gamma$ production at the LHC in NNLO QCD,” *JHEP* **2015** (2015) 85, arXiv:1504.01330, doi:10.1007/JHEP07(2015)085.

- [11] L3 Collaboration, “Study of the $e^+e^- \rightarrow Z\gamma$ process at LEP and limits on triple neutral-gauge-boson couplings,” *Phys. Lett. B* **597** (2004) 119, doi:10.1016/j.physletb.2004.07.002.
- [12] V. Abazov *et al.*, “Measurement of the $Z\gamma \rightarrow \nu\bar{\nu}\gamma$ Production Cross Section and Limits on Anomalous $ZZ\gamma$ and $Z\gamma\gamma$ Couplings in $p\bar{p}$ Collisions at $\sqrt{s} = 1.96$ TeV,” *Phys. Rev. Lett.* **102** (2009) 201802, doi:10.1103/PhysRevLett.102.201802.
- [13] V. Khachatryan *et al.*, “Measurement of the $Z\gamma \rightarrow \nu\bar{\nu}\gamma$ production cross section in pp collisions at $\sqrt{s} = 8$ TeV and limits on anomalous $ZZ\gamma$ and $Z\gamma\gamma$ trilinear gauge boson couplings,” *Phys. Lett. B* **760** (2016) 448, arXiv:1602.07152, doi:10.1016/j.physletb.2016.06.080.
- [14] M. Grazzini, S. Kallweit, and M. Wiesemann, “Fully differential NNLO computations with MATRIX,” *EPJ C* **78** (2018) 537, arXiv:1711.06631, doi:10.1140/epjc/s10052-018-5771-7.
- [15] M. Aaboud *et al.*, “Measurement of the $Z\gamma \rightarrow \nu\bar{\nu}\gamma$ production cross section in pp Collisions at $\sqrt{s} = 13$ TeV with the ATLAS detector and limits on anomalous triple gauge-boson couplings,” arXiv:1810.04995.
- [16] T. Gleisberg *et al.*, “Event generation with SHERPA 1.1,” *JHEP* **2009** (2009) 007, arXiv:0811.4622, doi:10.1088/1126-6708/2009/02/007.
- [17] J. Campbell, R. Ellis, and C. Williams, “Vector boson pair production at the LHC,” *JHEP* **2011** (2011) 18, arXiv:1105.0020, doi:10.1007/JHEP07(2011)018.
- [18] K. Hagiwara, R. Peccei, D. Zeppenfeld, and K. Hikasa, “Probing the weak boson sector in $e^+e^- \rightarrow W^+W^-$,” *Nucl. Phys.* **282** (1987) 253, doi:10.1016/0550-3213(87)90685-7.
- [19] U. Baur and E. Berger, “Probing the weak boson sector in $Z\gamma$ production at hadron colliders,” *Phys. Rev. D* **47** (1993) 4889, doi:10.1103/PhysRevD.47.4889.
- [20] U. Baur and D. Rainwater, “Probing neutral gauge boson self-interactions in ZZ production at hadron colliders,” *Phys. Rev. D* **62** (2000) 113011, arXiv:hep-ph/0008063, doi:10.1103/PhysRevD.62.113011.

- [21] S. Chatrchyan *et al.*, “Measurement of the $W\gamma$ and $Z\gamma$ inclusive cross sections in pp collisions at $\sqrt{s} = 7$ TeV and limits on anomalous triple gauge boson couplings,” *Phys. Rev. D* **89** (2014) 092005, [arXiv:1308.6832](#), [doi:10.1103/PhysRevD.89.092005](#).
- [22] S. Chatrchyan *et al.*, “Measurement of the production cross section for $Z\gamma \rightarrow \nu\bar{\nu}\gamma$ in pp collisions at $\sqrt{s} = 7$ TeV and limits on $ZZ\gamma$ and $Z\gamma\gamma$ triple gauge boson couplings,” *JHEP* **10** (2013) 164, [arXiv:1309.1117](#), [doi:10.1007/JHEP10\(2013\)164](#).
- [23] D. Green, P. Meade, and M. Pleier, “Multiboson interactions at the LHC,” *Rev. Mod. Phys.* **89** (2017) 035008, [arXiv:1610.07572](#), [doi:10.1103/RevModPhys.89.035008](#).
- [24] The ALEPH Collaboration, The DELPHI collaboration, The L3 Collaboration, The OPAL Collaboration, and The LEP Electroweak Working Group, “Electroweak measurements in electron-positron collisions at W-boson-pair energies at LEP,” *Phys. Rep.* **532** (2013) 119, [arXiv:1302.3415](#), [doi:10.1016/j.physrep.2013.07.004](#).
- [25] T. Aaltonen *et al.*, “Limits on Anomalous Trilinear Gauge Couplings in $Z\gamma$ Events from $p\bar{p}$ Collisions at $\sqrt{s} = 1.96$ TeV,” *Phys. Rev. Lett.* **107** (2011) 051802, [arXiv:1103.2990](#), [doi:10.1103/PhysRevLett.107.051802](#).
- [26] V. Abazov *et al.*, “ $Z\gamma$ production and limits on anomalous $ZZ\gamma$ and $Z\gamma\gamma$ couplings in $p\bar{p}$ collisions at $\sqrt{s} = 1.96$ TeV,” *Phys. Rev. D* **85** (2012) 052001, [arXiv:1111.3684](#), [doi:10.1103/PhysRevD.85.052001](#).
- [27] N. Ashby, “Relativity in the Global Positioning System,” *Living Rev. Relativ.* **6** (2003) 1, [doi:10.12942/lrr-2003-1](#).
- [28] N. Aghanim *et al.*, “Planck 2018 results. VI. Cosmological parameters,” [arXiv:1807.06209](#).
- [29] R. Wald, *General Relativity*. University of Chicago Press, 1984.
- [30] B. Abbott *et al.*, “Observation of Gravitational Waves from a Binary Black Hole Merger,” *Phys. Rev. Lett.* **116** (2016) 061102, [arXiv:1602.03837](#), [doi:10.1103/PhysRevLett.116.061102](#).

- [31] B. Abbott *et al.*, “Tests of general relativity with GW150914,” *Phys. Rev. Lett.* **116** (2016) 221101, [arXiv:1602.03841](#), [doi:10.1103/PhysRevLett.116.221101](#).
- [32] P. van Dokkum *et al.*, “A galaxy lacking dark matter,” *Nature* **555** (2018) 629, [arXiv:1803.10237](#), [doi:10.1038/nature25767](#).
- [33] M. Bartelmann and M. Maturi, “Weak gravitational lensing,” [arXiv:1612.06535](#).
- [34] P. Natarajan *et al.*, “Mapping substructure in the HST Frontier Fields cluster lenses and in cosmological simulations,” *Monthly Notices of the Royal Astronomical Society* **468** (2017) 1962, [arXiv:1702.04348](#), [doi:10.1093/mnras/stw3385](#).
- [35] S. Allen, A. Evrard, and A. Mantz, “Cosmological Parameters from Observations of Galaxy Clusters,” *ARAA* **49** (2011) 409, [arXiv:1103.4829](#), [doi:10.1146/annurev-astro-081710-102514](#).
- [36] V. Springel *et al.*, “Simulating the joint evolution of quasars, galaxies and their large-scale distribution,” *Nature* **435** (2005) 629, [arXiv:astro-ph/0504097](#), [doi:10.1038/nature03597](#).
- [37] D. Clowe *et al.*, “A direct empirical proof of the existence of dark matter,” *Astrophys. J.* **648** (2006) L109, [arXiv:astro-ph/0608407](#), [doi:10.1086/508162](#).
- [38] J. de Swart, G. Bertone, and J. van Dongen, “How dark matter came to matter,” *Nature Astr.* **1** (2017) 0059, [arXiv:1703.00013](#), [doi:10.1038/s41550-017-0059](#).
- [39] G. Bertone, D. Hooper, and J. Silk, “Particle dark matter: evidence, candidates and constraints,” *Phys. Rep.* **405** (2005) 279, [arXiv:hep-ph/0404175](#), [doi:10.1016/j.physrep.2004.08.031](#).
- [40] R. Gaitskell, “Direct Detection of Dark Matter,” *Annu. Rev. Nucl. Part. Sci.* **54** (2004) 315, [doi:10.1146/annurev.nucl.54.070103.181244](#).
- [41] L. Baudis, “The Search for Dark Matter,” *Eur. Rev.* **26** (2018) 70, [arXiv:1801.08128](#), [doi:10.1017/S1062798717000783](#).

- [42] A. Nelson *et al.*, “Confronting the Fermi Line with LHC data: an Effective Theory of Dark Matter Interaction with Photons,” *Phys. Rev. D* **89** (2014) 056011, [arXiv:1307.5064](https://arxiv.org/abs/1307.5064), doi:10.1103/PhysRevD.89.056011.
- [43] C. Degrande *et al.*, “Effective field theory: A modern approach to anomalous couplings,” *Annals of Phys.* **335** (2013) 21, [arXiv:1205.4231](https://arxiv.org/abs/1205.4231), doi:10.1016/j.aop.2013.04.016.
- [44] D. Abercrombie *et al.*, “Dark Matter Benchmark Models for Early LHC Run-2 Searches: Report of the ATLAS/CMS Dark Matter Forum,” [arXiv:1507.00966](https://arxiv.org/abs/1507.00966).
- [45] G. Busoni *et al.*, “Recommendations on presenting LHC searches for missing transverse energy signals using simplified s -channel models of dark matter,” [arXiv:1603.04156](https://arxiv.org/abs/1603.04156).
- [46] V. Khachatryan *et al.*, “Search for new phenomena in monophoton final states in proton-proton collisions at $\sqrt{s} = 8$ TeV,” *Phys. Lett. B* **755** (2016) 102, [arXiv:1410.8812](https://arxiv.org/abs/1410.8812), doi:10.1016/j.physletb.2016.01.057.
- [47] G. Aad *et al.*, “Search for new phenomena in events with a photon and missing transverse momentum in pp collisions at $\sqrt{s} = 8$ TeV with the ATLAS detector,” *Phys. Rev. D* **91** (2015) 012008, [arXiv:1411.1559](https://arxiv.org/abs/1411.1559), doi:10.1103/PhysRevD.91.012008.
- [48] Albert, A. on behalf of the CMS Collaboration, “Searches for dark matter with CMS.” ICHEP 2018, 2018.
- [49] A. Sirunyan *et al.*, “Search for new physics in events with a leptonically decaying Z boson and a large transverse momentum imbalance in proton-proton collisions at $\sqrt{s} = 13$ TeV,” *Eur. Phys. J. C* **78** (2018) 291, [arXiv:1711.00431](https://arxiv.org/abs/1711.00431), doi:10.1140/epjc/s10052-018-5740-1.
- [50] A. Sirunyan *et al.*, “Search for new physics in final states with an energetic jet or a hadronically decaying W or Z boson and transverse momentum imbalance at $\sqrt{s} = 13$ TeV,” *Phys. Rev. D* **97** (2018) 092005, [arXiv:1712.02345](https://arxiv.org/abs/1712.02345), doi:10.1103/PhysRevD.97.092005.

- [51] A. Sirunyan *et al.*, “Search for new physics in final states with a single photon and missing transverse momentum in proton-proton collisions at $\sqrt{s} = 13$ TeV,” [arXiv:1810.00196](https://arxiv.org/abs/1810.00196).
- [52] A. Sirunyan *et al.*, “Search for new physics in the monophoton final state in proton-proton collisions at $\sqrt{s} = 13$ TeV,” *JHEP* **2017** (2017) 73, [arXiv:1706.03794](https://arxiv.org/abs/1706.03794), doi:10.1007/JHEP10(2017)073.
- [53] M. Aaboud *et al.*, “Search for dark matter at $\sqrt{s} = 13$ TeV in final states containing an energetic photon and large missing transverse momentum with the ATLAS detector,” *Eur. Phys. J. C* **77** (2017) 393, [arXiv:1704.03848](https://arxiv.org/abs/1704.03848), doi:10.1140/epjc/s10052-017-4965-8.
- [54] C. Amole *et al.*, “Dark Matter Search Results from the PICO-60 C_3F_8 Bubble Chamber,” *Phys. Rev. Lett.* **118** (2017) 251301, [arXiv:1702.07666](https://arxiv.org/abs/1702.07666), doi:10.1103/PhysRevLett.118.251301.
- [55] D. Akerib *et al.*, “Results on the Spin-Dependent Scattering of Weakly Interacting Massive Particles on Nucleons from the Run 3 Data of the LUX Experiment,” *Phys. Rev. Lett.* **116** (2016) 161302, [arXiv:1602.03489](https://arxiv.org/abs/1602.03489), doi:10.1103/PhysRevLett.116.161302.
- [56] A. Tan *et al.*, “Dark Matter Results from First 98.7 Days of Data from the PandaX-II Experiment,” *Phys. Rev. Lett.* **117** (2016) 121303, [arXiv:1607.07400](https://arxiv.org/abs/1607.07400), doi:10.1103/PhysRevLett.117.121303.
- [57] D. Akerib *et al.*, “Results from a search for dark matter in the complete LUX exposure,” *Phys. Rev. Lett.* **118** (2017) 021303, [arXiv:1608.07648](https://arxiv.org/abs/1608.07648), doi:10.1103/PhysRevLett.118.021303.
- [58] G. Angloher *et al.*, “Results on light dark matter particles with a low-threshold CRESST-II detector,” *Eur. Phys. J. C* **76** (2016) 25, [arXiv:1509.01515](https://arxiv.org/abs/1509.01515), doi:10.1140/epjc/s10052-016-3877-3.
- [59] R. Agnese *et al.*, “New Results from the Search for Low-Mass Weakly Interacting Massive Particles with the CDMS Low Ionization Threshold Experiment,” *Phys. Rev. Lett.* **116** (2016) 071301, [arXiv:1509.02448](https://arxiv.org/abs/1509.02448), doi:10.1103/PhysRevLett.116.071301.

- [60] N. Arkani-Hamed, S. Dimopoulos, and G. Dvali, “The hierarchy problem and new dimensions at a millimeter,” *Phys. Lett. B* **429** (1998) 263, [arXiv:hep-ph/9803315](#), doi:10.1016/S0370-2693(98)00466-3.
- [61] J. Murata and S. Tanaka, “A review of short-range gravity experiments in the LHC era,” *Class. Quant. Grav.* **32** (2015) 033001, [arXiv:1408.3588](#), doi:10.1088/0264-9381/32/3/033001.
- [62] G. Giudice, R. Rattazzi, and J. Wells, “Quantum gravity and extra dimensions at high-energy colliders,” *Nucl. Phys. B* **544** (1999) 3, [arXiv:hep-ph/9811291](#), doi:10.1016/S0550-3213(99)00044-9.
- [63] S. Ask, “Search For Extra Dimensions At LEP,” *Proceedings of the 32nd International Conference on High-Energy Physics* (2005) 1289, [arXiv:hep-ex/0410004](#), doi:10.1142/9789812702227_0266.
- [64] T. Aaltonen *et al.*, “Search for Large Extra Dimensions in Final States Containing One Photon or Jet and Large Missing Transverse Energy Produced in $p\bar{p}$ Collisions at $\sqrt{s} = 1.96$ TeV,” *Phys. Rev. Lett.* **101** (2008) 181602, [arXiv:0807.3132](#), doi:10.1103/PhysRevLett.101.181602.
- [65] G. Aad *et al.*, “Search for new phenomena with the monojet and missing transverse momentum signature using the ATLAS detector in $\sqrt{s} = 7$ TeV proton-proton collisions,” *Phys. Lett. B* **705** (2011) 294, [arXiv:1106.5327](#), doi:10.1016/j.physletb.2011.10.006.
- [66] G. Aad *et al.*, “Search for dark matter candidates and large extra dimensions in events with a photon and missing transverse momentum in pp collision data at $\sqrt{s} = 7$ TeV with the ATLAS detector,” *Phys. Rev. Lett.* **110** (2013) 011802, [arXiv:1209.4625](#), doi:10.1103/PhysRevLett.110.011802.
- [67] J. Hoskins *et al.*, “Experimental tests of the gravitational inverse-square law for mass separations from 2 to 105 cm,” *Phys. Rev. D* **32** (1985) 3084, doi:10.1103/PhysRevD.32.3084.
- [68] R. Spero *et al.*, “Test of the Gravitational Inverse-Square Law at Laboratory Distances,” *Phys. Rev. Lett.* **44** (1980) 1645, doi:10.1103/PhysRevLett.44.1645.

- [69] D. Kapner *et al.*, “Tests of the Gravitational Inverse-Square Law below the Dark-Energy Length Scale,” *Phys. rev. Lett.* **98** (2007) 021101, arXiv:hep-ph/0611184, doi:10.1103/PhysRevLett.98.021101.
- [70] A. Geraci *et al.*, “Improved constraints on non-Newtonian forces at 10 microns,” *Phys. Rev. D* **78** (2008) 022002, arXiv:0802.2350, doi:10.1103/PhysRevD.78.022002.
- [71] S. Tanaka *et al.*, “Search of non-standard strong gravity at nuclear scale using electron spin geodetic precession,” *EPJ Web of Conferences* **66** (2014) 05021, doi:10.1051/epjconf/20146605021.
- [72] L. Evans and P. Bryant, “LHC Machine,” *JINST* **3** (2008) S08001, doi:10.1088/1748-0221/3/08/S08001.
- [73] G. Aad *et al.*, “The ATLAS Experiment at the CERN Large Hadron Collider,” *JINST* **3** (2008) S08003, doi:10.1088/1748-0221/3/08/S08003.
- [74] K. Aamodt *et al.*, “The ALICE experiment at the CERN LHC,” *JINST* **3** (2008) S08002, doi:10.1088/1748-0221/3/08/S08002.
- [75] S. Chatrchyan *et al.*, “The CMS experiment at the CERN LHC,” *JINST* **3** (2008) S08004, doi:10.1088/1748-0221/3/08/S08004.
- [76] A. Alves *et al.*, “The LHCb Detector at the LHC,” *JINST* **3** (2008) S08005, doi:10.1088/1748-0221/3/08/S08005.
- [77] E. Quaranta *et al.*, “Modeling of beam-induced damage of the LHC tertiary collimators,” *Phys. Rev. Accel. Beams* **20** (2017) 091002, doi:10.1103/PhysRevAccelBeams.20.091002.
- [78] K. Wille, *The Physics of Particle Accelerators*. Oxford University Press, 2000.
- [79] H. Schopper, *LEP - The Lord of the Collider Rings at CERN 1980-2000*. Springer-Verlag Berlin Heiderlberg, 2009. doi:10.1007/978-3-540-89301-1.
- [80] V. Lebedev and V. Shiltsev, *Accelerator Physics at the Tevatron Collider*. Springer-Verlag New York, 2014. doi:10.1007/978-1-4939-0885-1.

- [81] W. Wittmer, A. Verdier, and F. Zimmermann, “Correcting the LHC β^* at collision,” *Proceedings of the 2003 Particle Accelerator Conference* **4** (2003) 2237, doi:10.1109/PAC.2003.1289077.
- [82] R. Bruce, R. Assmann, and S. Redaelli, “Calculations of safe collimator settings and β^* at the CERN Large Hadron Collider,” *Phys. Rev. Accel. Beams* **18** (2015) 061001, doi:10.1103/PhysRevSTAB.18.061001.
- [83] S. Orfanelli *et al.*, “A novel Beam Halo Monitor for the CMS experiment at the LHC,” *JINST* **10** (2015) P11011, doi:10.1088/1748-0221/10/11/P11011.
- [84] S. Chatrchyan *et al.*, “Precise Mapping of the Magnetic Field in the CMS Barrel Yoke using Cosmic Rays,” *JINST* **5** (2010) T03021, arXiv:0910.5530, doi:10.1088/1748-0221/5/03/T03021.
- [85] D. Petyt, “Mitigation of Anomalous APD signals in the CMS Electromagnetic Calorimeter,” *J. Phys. Conf. Series* **404** (2012) 012043, doi:10.1088/1742-6596/404/1/012043.
- [86] A. Farzanehfar, “Mitigating high energy anomalous signals in the CMS barrel Electromagnetic Calorimeter.” Presentation at 30 June ECAL upgrade meeting, 2015.
- [87] M. Dejardin, “Discussion on the limit of the performances of possible ECAL barrel electronics due to the increase of APD leakage current at HL-LHC.” CMS DN-2015/014, 2015.
- [88] S. van der Meer, “Calibration of the effective beam height in the ISR.” CERN-ISR-PO-68-31, 1968.
- [89] CMS Collaboration, “CMS luminosity measurements for the 2016 data-taking period.” CMS-PAS-LUM-17-001, 2017.
- [90] V. Gribov and L. Lipatov, “Deep inelastic electron scattering in perturbation theory,” *Phys. Lett. B* **37** (1971) 78, doi:10.1016/0370-2693(71)90576-4.
- [91] Y. Dokshitzer, “Calculation of the Structure Functions for Deep Inelastic Scattering and e+ e- Annihilation by Perturbation Theory in Quantum Chromodynamics,” *Sov.Phys.JETP* **46** (1977) 641.

- [92] G. Altarelli and G. Parisi, “Asymptotic freedom in parton language,” *Nucl. Phys. B.* **126** (1977) 298, doi:10.1016/0550-3213(77)90384-4.
- [93] J. Campbell, J. Huston, and W. Stirling, “Hard Interactions of Quarks and Gluons: a Primer for LHC Physics,” *Rept. Prog. Phys.* **70** (2007) 89, arXiv:hep-ph/0611148, doi:10.1088/0034-4885/70/1/R02.
- [94] R. Ball *et al.*, “Parton distributions for the LHC run II,” *JHEP* **2015** (2015) 40, arXiv:1410.8849, doi:10.1007/JHEP04(2015)040.
- [95] R. Ball *et al.*, “Parton distributions from high-precision collider data,” *EPJ C* **77** (2017) 663, arXiv:1706.00428, doi:10.1140/epjc/s10052-017-5199-5.
- [96] J. Bendavid, “New MC Features for Analysis in 74x Plus more details on scale/PDF uncertainties.” Presentation at 4 November PPD general meeting, 2015.
- [97] J. Alwall *et al.*, “The automated computation of tree-level and next-to-leading order differential cross sections, and their matching to parton shower simulations,” *JHEP* **2014** (2014) 79, arXiv:1405.0301, doi:10.1007/JHEP07(2014)079.
- [98] J. Butterworth *et al.*, “PDF4LHC recommendations for LHC Run II,” *J. Phys. G: Nucl. Part. Phys.* **43** (2016) 023001, arXiv:1510.03865, doi:10.1088/0954-3899/43/2/023001.
- [99] S. Catani, D. de Florian, G. Ferrera, and M. Grazzini, “Vector boson production at hadron colliders: transverse-momentum resummation and leptonic decay,” *JHEP* **2015** (2015) arXiv:1507.06937, doi:10.1007/JHEP12(2015)047.
- [100] T. Sjöstrand *et al.*, “An introduction to PYTHIA 8.2,” *Comp. Phys. Comm.* **191** (2015) 159, arXiv:1410.3012, doi:10.1016/j.cpc.2015.01.024.
- [101] V. Khachatryan *et al.*, “Event generator tunes obtained from underlying event and multiparton scattering measurements,” *Eur. Phys. J. C* **76** (2016) 155, arXiv:1512.00815, doi:10.1140/epjc/s10052-016-3988-x.
- [102] S. Agostinelli *et al.*, “GEANT4—a simulation toolkit,” *Nucl. Inst. Meth. A* **506** (2003) 250, doi:10.1016/S0168-9002(03)01368-8.

- [103] A. Sirunyan *et al.*, “Particle-flow reconstruction and global event description with the CMS detector,” *JINST* **12** (2017) P10003, [arXiv:1706.04965](https://arxiv.org/abs/1706.04965), doi:10.1088/1748-0221/12/10/P10003.
- [104] G. Bayatian *et al.*, “CMS Physics: Technical Design Report Volume 1: Detector Performance and Software.” CMS-TDR-8-1, 2006.
- [105] P. Adzic *et al.*, “Energy Resolution of the Barrel of the CMS Electromagnetic Calorimeter,” *JINST* **2** (2007) P04004, doi:10.1088/1748-0221/2/04/P04004.
- [106] V. Khachatryan *et al.*, “Performance of electron reconstruction and selection with the CMS detector in proton-proton collisions as $\sqrt{s} = 8$ TeV,” *JINST* **10** (2015) [arXiv:1502.02701](https://arxiv.org/abs/1502.02701), doi:10.1088/1748-0221/10/06/P06005.
- [107] V. Khachatryan *et al.*, “Performance of photon reconstruction and identification with the CMS detector in proton-proton collisions at $\sqrt{s} = 8$ TeV,” *JINST* **10** (2015) P08010, [arXiv:1502.02702](https://arxiv.org/abs/1502.02702), doi:10.1088/1748-0221/10/08/P08010.
- [108] S. Chatrchyan *et al.*, “Description and performance of track and primary-vertex reconstruction with the CMS tracker,” *JINST* **9** (2014) P10009, [arXiv:1405.6569](https://arxiv.org/abs/1405.6569), doi:10.1088/1748-0221/9/10/P10009.
- [109] Jain, S. on behalf of the EGM group, “PF cluster regression in Egamma.” Presentation at 20 November Particle flow study group meeting, 2018.